Available online at www.sciencedirect.com
SCIENCE DIRECT
Journal of Sound and Vibration 294 (2006) 678–705
JOURNAL OF SOUND AND VIBRATION
www.elsevier.com/locate/jsvi

A three-dimensional tunnel model for calculation of train-induced ground vibration

J.A. Forrest[a,*], H.E.M. Hunt[b]

[a]*Maritime Platforms Division, Defence Science & Technology Organisation, 506 Lorimer St, Fishermans Bend VIC 3207, Australia*
[b]*Department of Engineering, University of Cambridge, Trumpington Street, Cambridge CB2 1PZ, UK*

Received 4 March 2004; received in revised form 4 April 2005; accepted 3 December 2005
Available online 28 February 2006

Abstract

The frequency range of interest for ground vibration from underground urban railways is approximately 20 to 100 Hz. For typical soils, the wavelengths of ground vibration in this frequency range are of the order of the spacing of train axles, the tunnel diameter and the distance from the tunnel to nearby building foundations. For accurate modelling, the interactions between these entities therefore have to be taken into account. This paper describes an analytical three-dimensional model for the dynamics of a deep underground railway tunnel of circular cross-section. The tunnel is conceptualised as an infinitely long, thin cylindrical shell surrounded by soil of infinite radial extent. The soil is modelled by means of the wave equations for an elastic continuum. The coupled problem is solved in the frequency domain by Fourier decomposition into ring modes circumferentially and a Fourier transform into the wavenumber domain longitudinally. Numerical results for the tunnel and soil responses due to a normal point load applied to the tunnel invert are presented. The tunnel model is suitable for use in combination with track models to calculate the ground vibration due to excitation by running trains and to evaluate different track configurations.

1. Introduction

The transmission of ground vibration from underground railways into nearby buildings has become an important topic in a world where many underground railways operate in densely populated urban areas and people's tolerance of environmental disturbances such as noise and vibration is decreasing. The aim of this paper is to develop a mathematical model of an underground railway tunnel surrounded by soil. Combining this with floating-slab track models as described in a companion paper [1] allows the construction of a complete model of the track, tunnel and soil that takes into account the major dynamic characteristics of the three-dimensional (3D) system. Since analytical techniques are used, results from the overall model can be computed relatively fast compared to numerical techniques such as finite-element (FE) analysis. This facilitates rapid comparison of cases such as different track configurations.

*Corresponding author. Fax: +61 3 9626 8373.
E-mail addresses: james.forrest@dsto.defence.gov.au (J.A. Forrest), hemh@eng.cam.ac.uk (H.E.M. Hunt).

0022-460X/$ - see front matter © 2006 Elsevier Ltd. All rights reserved.
doi:10.1016/j.jsv.2005.12.032

Traffic-induced ground vibration can propagate into buildings, manifesting itself as both vibratory motion and re-radiated noise. The result is discomfort and annoyance for occupants rather than structural damage. Greer and Manning [2] give the problem frequency ranges as 30–250 Hz for re-radiated sound and 1–80 Hz for perceptible vibration. Data in Heckl et al. [3] shows that peak levels occur in the range 40–80 Hz. With a speed of about 200 m/s, shear waves in the ground will have a wavelength of 4 m at 50 Hz, about the middle of these ranges. This wavelength is of the order of the spacing of train axles, the tunnel diameter, and the distance from the tunnel to building foundations; therefore interaction between these entities cannot be ignored.

The thesis [4] provides a comprehensive survey of the empirical, analytical and numerical approaches which have been used to model ground vibration from both surface and underground railways. Here a review of the work on underground railways will be given.

Prediction of ground vibration from underground railways has often relied on empirical means. An approach based on transmission factors gleaned from a database of over 3000 measurements from various sites is utilised by Hood et al. [5]. Other methods, such as those in Kraemer [6] and Melke [7], rely on semi-empirical transmission laws in conjunction with impedances derived from simplified lumped-parameter models of the track and the receiving building. Trochides [8] compares laboratory measurements on a scaled-down tunnel-soil-building system to predictions from approximate impedance models combined with statistical energy analysis (SEA).

An analytical methodology for calculating ground-vibration propagation from underground railways using tunnel and building models of infinite length to simplify solution is presented by Hunt [9]. Balendra et al. [10] use a substructure technique, based on consideration of the two-dimensional (2D) wave equation, to create a cross-sectional model of a rigid tunnel and a rigid strip foundation embedded in a viscoelastic half-space. Kostarev [11] represents an underground tunnel as an acoustic waveguide in a half-space, implemented by defining a variation in wavespeed with depth. Metrikine and Vrouwenvelder [12] use a 2D representation of the tunnel as a beam buried in a viscoelastic layer with a rigid base to calculate surface vibration with constant, harmonic and random loads moving along the beam. Krylov [13] applies earlier work [14] on surface railways by assuming that the tunnel diameter is much smaller than the wavelength of low-frequency propagated waves, so that each sleeper in an underground track can be construed as a point load buried in a half-space. Zhu and Ødegaard [15] compare results from a 2D wave-propagation model of a horizontally stratified medium with a buried force to those from a cross-sectional FE model of a tunnel and measurements, finding reasonable agreement at large distances from the load; however, near the tunnel, the tunnel dynamics are quite significant. Guan and Moore [16] treat the interaction between two deep side-by-side circular tunnels by solving the 3D wave equations for two cylindrical cavities in an unbounded medium. Sheng et al. [17] develop a "discrete wavenumber fictitious force" method based on the moving Green's functions for a layered half-space and a cylinder of infinite length. They use this to model ground vibration for stationary and moving harmonic loads applied to circular lined and unlined tunnels. The method uses a wavenumber transformation in the longitudinal direction and a cylindrical-coordinate solution for the tunnel represented as a shell, and has the advantage over the boundary-element (BE) method of requiring Green's functions for displacements only and not tractions as well.

Numerical models include the 2D plane-strain FE model of Balendra et al. [18], which represents the cross-section of a Singaporean subway-soil-building system and utilises a viscous absorbing boundary. The tunnel and soil are modelled with solid elements, the multi-storey building as a framework of beam elements. Chua et al. [19] use this model to calculate the vibration reduction effected by soft railpads and floating-slab track, construing the train input as a line load determined from a lumped-mass model of wheel and track. Rücker and Said [20] use a similar model bounded with boundary elements to determine the effect of an open vibration-screening trench between tunnel and building, and of a stiff plate on the ground surface. Jones et al. [21] use a 2D FE-BE approach to model both a bored, circular tunnel with and without a lining, and a cut-and-cover tunnel of rectangular cross-section with and without extra foundation engineering. However, such 2D models ignore the longitudinal dynamics of the track and tunnel.

Wolf [22] uses a 3D finite-difference tunnel model to evaluate a light-rail system, but only calculates static results to give the approximate response at very low frequencies. Thornely-Taylor [23] describes the application of a finite-difference time-domain (FDTD) method to the 3D vibration modelling of arbitrary

systems with moving excitation sources, combining the approach with BE modelling to calculate far-field sound radiation. The model is validated against measurements of ground surface vibration for a light railway with twin-bored tunnels in a layered ground in Ref. [24]. In applying the FE method, Gardien and Stuit [25] note the computational constraints which preclude a full 3D FE model of an underground railway. Instead, they use a 3D static FE model of the tunnel to obtain equivalent Timoshenko beam parameters, which are then utilised in a 2D side-on beam model of the track with a mass-spring train model to calculate the under-sleeper force, which can then be fed to a 2D plane-strain FE propagation model of the tunnel cross-section. Andersen and Jones [26] compare the relative merits of two- and 3D coupled FE-BE models for a cut-and-cover double-track tunnel and a deep single-track tunnel, calculating surface ground vibration up to 80 Hz for loads applied directly to the tunnel floor. The conclusion is that, despite their computational cost which makes parametric study difficult, 3D models are required for absolute predictions and more accurate estimates of the effect of changes in tunnel structure and depth.

The computational drawbacks of general 3D FE-BE representations can be addressed by so-called ''two-and-a-half dimensional'' methods that can be applied to specific geometries. Sheng et al. [27] assume that a surface or underground railway system is homogeneous in the track direction, so that the cross-section is invariant. Discretisation with combined FE-BE is only required over the cross-section, which can therefore be arbitrary, while a Fourier transform is applied longitudinally to give the problem in terms of discrete wavenumbers in that direction. The approach is used to model vibration from both a surface railway on layered soil and a bored tunnel. Degrande et al. [28] and Clouteau et al. [29,30] take a slightly different approach, based on a method developed earlier by Clouteau et al. [31] for application to very long structures such as quay walls. They assume periodicity rather than invariance in the longitudinal direction, using a Floquet transformation instead of a Fourier one. This results in FE-BE discretisation being required only over a single bounded reference cell representing a section of the tunnel. Theoretical results for a shallow cut-and-cover masonry tunnel embedded in layers of sand in Paris and for a deep bored tunnel with periodic cast-iron lining in clay in London are given in Ref. [29], while computed and measured results for the Paris tunnel are compared in Ref. [28]. Detailed measurements of train, track, tunnel, soil and building vibration are given for the Paris site in Ref. [32] and for the London site in Ref. [33].

It can be seen that recent efforts have produced computationally feasible numerical models, which can represent the details of specific sites in three dimensions. However, the analytical models that exist are often only 2D, or fail to take the full tunnel dynamics into account, and all consider only simple loads applied directly to the tunnel or soil. None have included detailed track models directly coupled to a tunnel model. There is thus a need to develop a detailed 3D underground-railway model that includes the dynamics of the train, the track, the tunnel and the soil, with the advantages conferred by the use of an analytical approach. This paper presents an analytical model for the tunnel in soil. It describes work originally developed in Ref. [4]. The tunnel is conceptualised as an infinitely long, thin cylindrical shell surrounded by soil of infinite radial extent. The soil is treated by means of the wave equations for an elastic continuum. This means the model has no free surface, which would both reflect impinging body waves back towards the top of the tunnel and have surface waves excited upon it. In the far field, it is likely that buildings would receive more energy from such surface (Rayleigh) waves than from body waves, since the former decay less rapidly. Nevertheless, the surface would have much less influence on responses near the tunnel, especially the deeper the tunnel is. Such nearfield responses are of most importance in assessing the effectiveness of different track designs, where comparative energy input into the soil is of greatest interest. Therefore, despite the absence of a free soil surface, useful results concerning the propagation of vibration into the soil near the tunnel can be obtained.

2. Cylindrical shell equations

The tunnel is modelled as a cylindrical shell of infinite length. The following discussion will make use of the Flügge equations of motion for a thin cylindrical shell made of linear elastic, homogeneous and isotropic material. Such a shell is shown in Fig. 1(a). These equations can be obtained by adding inertia terms to the static equations given in Flügge [34], or from Leissa [35], who also discusses various other thin-shell theories. Each equation represents dynamic equilibrium in one of the three principal directions. Equilibrium in the

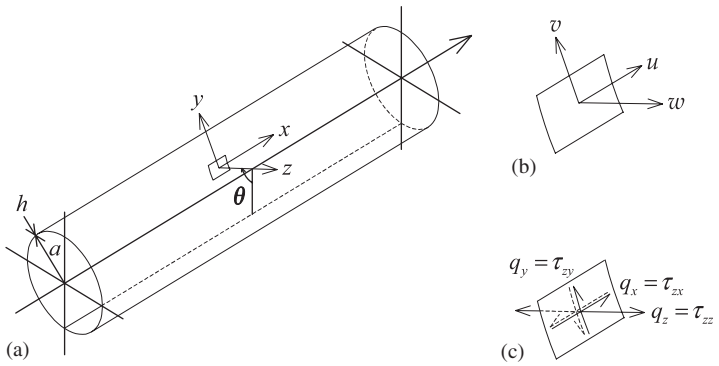

Fig. 1. Coordinate system used for the thin-walled cylindrical-shell theory, showing (a) the principle directions for a typical element in the shell, (b) the corresponding displacement components and (c) the corresponding surface stress components. To model a railway tunnel, the length of the cylindrical shell is taken as infinite.

longitudinal direction x gives

$$a\frac{\partial^2 u}{\partial x^2}+\frac{(1-\nu)}{2a}\frac{\partial^2 u}{\partial \theta^2}+\frac{(1+\nu)}{2}\frac{\partial^2 v}{\partial x\,\partial\theta}-\nu\frac{\partial w}{\partial x}+\frac{h^2}{12}\left[\frac{(1-\nu)}{2a^3}\frac{\partial^2 u}{\partial\theta^2}+\frac{\partial^3 w}{\partial x^3}-\frac{(1-\nu)}{2a^2}\frac{\partial^3 w}{\partial x\,\partial\theta^2}\right]+a\frac{(1-\nu^2)}{Eh}q_x-\rho a\frac{(1-\nu^2)}{E}\frac{\partial^2 u}{\partial t^2}=0, \tag{1}$$

equilibrium in the tangential direction y gives

$$\frac{(1+\nu)}{2}\frac{\partial^2 u}{\partial x\,\partial\theta}+a\frac{(1-\nu)}{2}\frac{\partial^2 v}{\partial x^2}+\frac{1}{a}\frac{\partial^2 v}{\partial\theta^2}-\frac{1}{a}\frac{\partial w}{\partial\theta}+\frac{h^2}{12}\left[\frac{3(1-\nu)}{2a}\frac{\partial^2 v}{\partial x^2}+\frac{(3-\nu)}{2a}\frac{\partial^3 w}{\partial x^2\,\partial\theta}\right]+a\frac{(1-\nu^2)}{Eh}q_y-\rho a\frac{(1-\nu^2)}{E}\frac{\partial^2 v}{\partial t^2}=0, \tag{2}$$

and equilibrium in the radial direction z gives

$$\nu\frac{\partial u}{\partial x}+\frac{1}{a}\frac{\partial v}{\partial\theta}-\frac{1}{a}w-\frac{h^2}{12}\left[a\frac{\partial^4 w}{\partial x^4}+\frac{2}{a}\frac{\partial^4 w}{\partial x^2\,\partial\theta^2}+\frac{1}{a^3}\frac{\partial^4 w}{\partial\theta^4}\right]-\frac{h^2}{12}\left[\frac{\partial^3 u}{\partial x^3}-\frac{(1-\nu)}{2a^2}\frac{\partial^3 u}{\partial x\,\partial\theta^2}+\frac{(3-\nu)}{2a}\frac{\partial^3 v}{\partial x^2\,\partial\theta}+\frac{1}{a^3}w+\frac{2}{a^3}\frac{\partial^2 w}{\partial\theta^2}\right]+a\frac{(1-\nu^2)}{Eh}q_z-\rho a\frac{(1-\nu^2)}{E}\frac{\partial^2 w}{\partial t^2}=0, \tag{3}$$

where u, v and w are the displacement components in directions x, y and z, respectively and varying with time t, a is the radius of the shell, and h is its thickness. The terms in Eqs. (1)–(3) which are multiplied by the factor $h^2/12$ represent the contribution of bending effects to the displacements, while those without represent the contribution of membrane effects. The shell material has Young's modulus E, Poisson's ratio ν, and density ρ. The effects of material damping can be included by using complex material parameters in the frequency domain. The net applied loading is usually represented by stress components acting on the inside surface of the shell: two shear tractions q_x and q_y, and one normal stress q_z. More precisely, these are the net stresses acting, the differences between the inside and outside values of the surface stresses τ_{zx}, τ_{zy} and τ_{zz}, respectively. The displacement and stress components are shown in Fig. 1(b) and (c).

If the loading applied to an infinitely long cylindrical shell comprises stress components which are harmonic in both space and time, of the form

$$\begin{aligned} q_x(x,t) &= \tilde{Q}_{xn} \cos n\theta \, e^{i(\omega t+\xi x)}, \\ q_y(x,t) &= \tilde{Q}_{yn} \sin n\theta \, e^{i(\omega t+\xi x)}, \\ q_z(x,t) &= \tilde{Q}_{zn} \cos n\theta \, e^{i(\omega t+\xi x)}, \end{aligned} \tag{4}$$

and hence separable in time t, space x and angular position θ, then the equations of motion (1)–(3) are satisfied by the similarly harmonic displacement components

$$\begin{aligned} u(x,t) &= \tilde{U}_n \cos n\theta \, e^{i(\omega t+\xi x)}, \\ v(x,t) &= \tilde{V}_n \sin n\theta \, e^{i(\omega t+\xi x)}, \\ w(x,t) &= \tilde{W}_n \cos n\theta \, e^{i(\omega t+\xi x)}, \end{aligned} \tag{5}$$

where ω is angular frequency, ξ is angular wavenumber, and n is a positive integer, while the tilde on the uppercase coefficients $\tilde{Q}_{xn}$, $\tilde{Q}_{yn}$, $\tilde{Q}_{zn}$, $\tilde{U}_n$, $\tilde{V}_n$ and $\tilde{W}_n$ indicate that they are in the wavenumber domain as well as the frequency domain. The spatial exponential term $e^{i\xi x}$ arises because of the cylindrical shell's infinite longitudinal extent; if it was of finite length L, then these exponentials would be replaced by terms like $\sin(m\pi x/L)$ or $\cos(m\pi x/L)$ with m a positive integer. The trigonometric terms represent ring modes of the cylindrical cross-section and are chosen so that the displacements are symmetric about $\theta = 0$, the downward vertical. Fig. 2 shows these ring modes as they relate to the three displacement components u, v and w. The modes are composed of an integer number n of waves developed around the circumference. Hence for the in-plane flexural modes of Fig. 2(a), which are associated with radial displacement w, $n = 0$ corresponds to an expansion or "breathing" mode, $n = 1$ corresponds to one full wave or translation of the cross-section, $n = 2$ corresponds to two full waves or a squashed cross-section, and so on. The ring modes for the tangential displacement v are the in-plane extensional modes of Fig. 2(b), while those for the longitudinal displacement u are the out-of-plane flexural modes of Fig. 2(c). The plane referred to is that of the ring; from a shell point of view, w comprises mostly out-of-plane flexural motion, while u and v comprise mostly in-plane extensional motion. It should also be noted that because of the choice of $\sin n\theta$ to describe the circumferential variation of v, the current formulation ignores the simple torsional mode (or rigid-body ring rotation) that would correspond to $n = 0$.

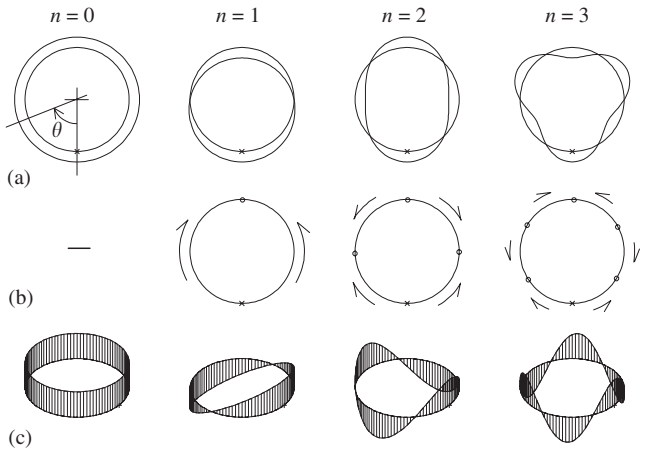

Fig. 2. (a) In-plane flexural ring modes, varying as $\cos n\theta$ and corresponding to radial displacement w; (b) in-plane extensional ring modes, varying as $\sin n\theta$ and corresponding to tangential displacement v; and (c) out-of-plane flexural ring modes, varying as $\cos n\theta$ and corresponding to longitudinal displacement u, for different values of circumferential modenumber n. The $\theta = 0$ points are marked with small crosses on the undeformed ring shapes, while the small circles in (b) mark the additional nodal points on the ring's circumference.

Substitution of the stresses (4) and displacements (5) into Eqs. (1)–(3) and putting all three equations into matrix form yields

$$[\mathbf{A}]\begin{Bmatrix}\tilde{U}_n\\ \tilde{V}_n\\ \tilde{W}_n\end{Bmatrix}=\frac{-a(1-\nu^2)}{Eh}\begin{Bmatrix}\tilde{Q}_{xn}\\ \tilde{Q}_{yn}\\ \tilde{Q}_{zn}\end{Bmatrix}, \tag{6}$$

where $[\mathbf{A}]$ is a matrix of coefficients whose elements are given in Appendix A.1. If the stresses $\tilde{\mathbf{Q}}_n = \{\tilde{Q}_{xn} \quad \tilde{Q}_{yn} \quad \tilde{Q}_{zn}\}^{\mathrm{T}}$ are such that they represent some kind of unit loading condition, then the displacements $\tilde{\mathbf{U}}_n = \{\tilde{U}_n \quad \tilde{V}_n \quad \tilde{W}_n\}^{\mathrm{T}}$ represent the displacement frequency-response functions (FRFs) in the wavenumber domain for a particular circumferential mode n. The actual stresses and displacements will in general be linear combinations of the modal quantities.

3. Elastic continuum equations

The soil surrounding the tunnel is modelled as a 3D, homogeneous, isotropic elastic solid in the form of a thick-walled cylinder with an inner diameter equal to the diameter of the tunnel, and an outer diameter of infinite extent, as shown in Fig. 3(a). The solution for the motion of this cylinder is based on the method employed by Gazis [36] to investigate the modes of thick-walled cylindrical shells and developed further by Köpke [37] to model the dynamics of buried undersea pipelines. Köpke's solution is general, but the results only consider the driving-point response of the pipe based on the translation mode of the pipe cross-section.

The wave equation describing motion within a 3D, homogeneous, isotropic, elastic, solid medium is derived by Graff [38] and is

$$(\lambda+\mu)\nabla\nabla\cdot\mathbf{u}+\mu\nabla^2\mathbf{u}+\rho\mathbf{f}=\rho\frac{\partial^2\mathbf{u}}{\partial t^2}, \tag{7}$$

where $\mathbf{u}$ is the displacement vector, $\mathbf{f}$ the vector of body forces, t is time, $\lambda = 2\nu G/(1-2\nu)$ and $\mu = E/2(\nu+1) = G$ are Lamé's elastic constants (where G is shear modulus, E Young's modulus, and ν Poisson's ratio) for the medium, and ρ is the medium's density. In this case, the only body forces acting are due to gravity; but since the desired solution is for vibration about an equilibrium position, they are ignored and $\mathbf{f}$ is correspondingly set to zero. The problem has cylindrical geometry, so the cylindrical coordinate system will be used. The coordinate, displacement and stress directions are given in Fig. 3. Note that this system is different from that used for the analysis of the cylindrical shell in the previous section, with z now denoting the longitudinal coordinate.

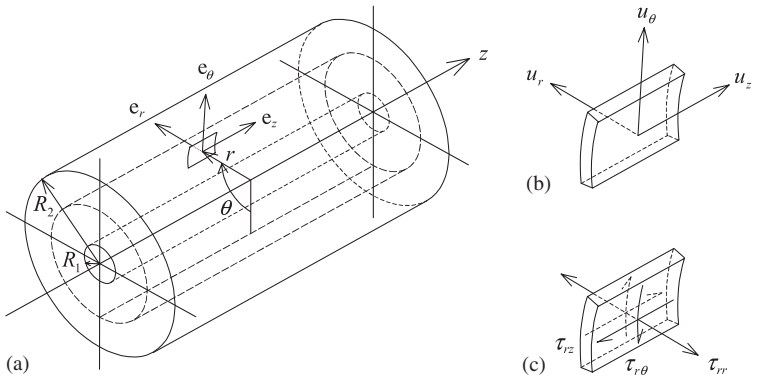

Fig. 3. Coordinate system used for the theory of an elastic continuum with cylindrical geometry, showing (a) the principle directions with their unit vectors for a typical element on a cylindrical surface of radius r within the bulk medium, (b) the corresponding displacement components and (c) the corresponding cylindrical-surface stress components (stresses acting on the edges of the element are not shown). To model the soil surrounding a railway tunnel, the inner radius is set to $R_1 = a$ to match the cylindrical shell of Fig. 1, the outer radius is made infinite $R_2 \to \infty$, and the length of the cylinder is taken as infinite.

The wave Eq. (7) can be solved by making use of the scalar and vector potentials—Lamé's potentials—which describe the field transformation

$$\mathbf{u} = \nabla\phi + \nabla \times \mathbf{H}, \quad \text{with} \quad \nabla \cdot \mathbf{H} = F(\mathbf{r}, t), \tag{8}$$

where $\mathbf{r}$ is the position vector (r, θ, z). The scalar function $F(\mathbf{r}, t)$ is arbitrary, due to the gauge invariance of the transformation. The property of gauge invariance essentially means that the displacement field is not altered by the choice of the potentials used to describe it. Usually $\mathbf{H}$ is defined by $\nabla \cdot \mathbf{H} = 0$ for convenience, but the arbitrary nature of $F(\mathbf{r}, t)$ will be useful for the current problem.

The displacement equation (7) is satisfied if the potentials satisfy

$$\nabla^2\phi = \frac{1}{c_1^2}\frac{\partial^2\phi}{\partial t^2} \quad \text{and} \quad \nabla^2\mathbf{H} = \frac{1}{c_2^2}\frac{\partial^2\mathbf{H}}{\partial t^2}, \tag{9}$$

where $c_1 = \sqrt{(\lambda + 2\mu)/\rho}$ is the speed of pressure waves in the medium and $c_2 = \sqrt{\mu/\rho}$ the speed of shear waves. Since there are no surfaces or interfaces in the bulk medium, only these two types of waves can exist. For cylindrical coordinates, the Laplacians in Eq. (9) are given by [38]

$$\begin{aligned}
\nabla^2\phi &= \frac{1}{r}\frac{\partial\phi}{\partial r} + \frac{\partial^2\phi}{\partial r^2} + \frac{1}{r^2}\frac{\partial^2\phi}{\partial\theta^2} + \frac{\partial^2\phi}{\partial z^2},\\
\nabla^2\mathbf{H} &= \left(\nabla^2 H_r - \frac{H_r}{r^2} - \frac{2}{r^2}\frac{\partial H_\theta}{\partial\theta}\right)\mathbf{e}_r + \left(\nabla^2 H_\theta - \frac{H_\theta}{r^2} + \frac{2}{r^2}\frac{\partial H_r}{\partial\theta}\right)\mathbf{e}_\theta + \nabla^2 H_z\mathbf{e}_z,
\end{aligned} \tag{10}$$

where $\mathbf{e}_r$, $\mathbf{e}_\theta$ and $\mathbf{e}_z$ are unit vectors in the principal directions of the cylindrical coordinate system, shown in Fig. 3(a), and H_r, H_θ and H_z are the components of $\mathbf{H}$.

From (8), the displacement components can be written out as

$$\begin{aligned}
u_r &= \frac{\partial\phi}{\partial r} + \frac{1}{r}\frac{\partial H_z}{\partial\theta} - \frac{\partial H_\theta}{\partial z},\\
u_\theta &= \frac{1}{r}\frac{\partial\phi}{\partial\theta} + \frac{\partial H_r}{\partial z} - \frac{\partial H_z}{\partial r},\\
u_z &= \frac{\partial\phi}{\partial z} + \frac{1}{r}\frac{\partial(rH_\theta)}{\partial r} - \frac{1}{r}\frac{\partial H_r}{\partial\theta}.
\end{aligned} \tag{11}$$

The components of stress τ_{jk} are given by the general stress–strain relation of Hooke's law, and are (see Ref. [39])

$$\begin{aligned}
\tau_{rr} &= (\lambda + 2\mu)\varepsilon_{rr} + \lambda\varepsilon_{\theta\theta} + \lambda\varepsilon_{zz},\\
\tau_{\theta\theta} &= \lambda\varepsilon_{rr} + (\lambda + 2\mu)\varepsilon_{\theta\theta} + \lambda\varepsilon_{zz},\\
\tau_{zz} &= \lambda\varepsilon_{rr} + \lambda\varepsilon_{\theta\theta} + (\lambda + 2\mu)\varepsilon_{zz},\\
\tau_{r\theta} &= 2\mu\varepsilon_{r\theta} = \tau_{\theta r},\\
\tau_{rz} &= 2\mu\varepsilon_{rz} = \tau_{zr},\\
\tau_{\theta z} &= 2\mu\varepsilon_{\theta z} = \tau_{z\theta},
\end{aligned} \tag{12}$$

where the standard convention for designating stress directions is used (a stress is considered positive if its direction and the direction of the normal to the surface it acts upon are either both positive or both negative with respect to the coordinate system). Hooke's law is valid for linear-elastic materials. If some damping is introduced into the material, so that it becomes viscoelastic, the stress–strain relations (12) are still valid for low damping and the small magnitudes of vibration considered here. The components of strain ε_{jk} are defined in cylindrical coordinates by [38]

$$\begin{aligned}
&\varepsilon_{rr} = \frac{\partial u_r}{\partial r}, \quad \varepsilon_{\theta\theta} = \frac{1}{r}\frac{\partial u_\theta}{\partial\theta} + \frac{u_r}{r}, \quad \varepsilon_{zz} = \frac{\partial u_z}{\partial z},\\
&\varepsilon_{r\theta} = \frac{1}{2}\left(\frac{1}{r}\frac{\partial u_r}{\partial\theta} + \frac{\partial u_\theta}{\partial r} - \frac{u_\theta}{r}\right), \quad \varepsilon_{\theta z} = \frac{1}{2}\left(\frac{\partial u_\theta}{\partial z} + \frac{1}{r}\frac{\partial u_z}{\partial\theta}\right),\\
&\varepsilon_{rz} = \frac{1}{2}\left(\frac{\partial u_r}{\partial z} + \frac{\partial u_z}{\partial r}\right).
\end{aligned} \tag{13}$$

Eqs. (7)–(13) supply enough information to solve for the displacement and stress components. To solve, solutions for the potentials in the wave Eq. (9), separable in the three space variables r, θ and z, and the time variable t, of the following form are assumed.

$$\begin{aligned}\phi &= f(r)\cos n\theta\, e^{i(\omega t+\xi x)},\\ H_r &= g_r(r)\sin n\theta\, e^{i(\omega t+\xi x)},\\ H_\theta &= g_\theta(r)\cos n\theta\, e^{i(\omega t+\xi x)},\\ H_z &= g_z(r)\sin n\theta\, e^{i(\omega t+\xi x)}.\end{aligned} \tag{14}$$

These represent harmonic solutions in the same way as those used in the cylindrical shell analysis, but now there is also variation with radius r governed by the functions f, g_r, g_θ and g_z (which also vary with ω, ξ and n). Substitution of solutions (14) into Eq. (9) making use of definitions (10) and considering each component of the equation in $\mathbf{H}$ in turn results in the four differential equations

$$\begin{aligned}&r^2f'' + rf' - \left[\left(\xi^2 - \frac{\omega^2}{c_1^2}\right)r^2 + n^2\right]f = 0,\\ &r^2g_r'' + rg_r' - \left[\left(\xi^2 - \frac{\omega^2}{c_2^2}\right)r^2 + n^2 + 1\right]g_r + 2ng_\theta = 0,\\ &r^2g_\theta'' + rg_\theta' - \left[\left(\xi^2 - \frac{\omega^2}{c_2^2}\right)r^2 + n^2 + 1\right]g_\theta + 2ng_r = 0,\\ &r^2g_z'' + rg_z' - \left[\left(\xi^2 - \frac{\omega^2}{c_2^2}\right)r^2 + n^2\right]g_z = 0,\end{aligned} \tag{15}$$

where prime denotes differentiation with respect to r.

The first and fourth of Eq. (15) are modified Bessel equations of order n (see Ref. [40]), and thus have solutions based on modified Bessel functions of order n. However, the second and third equations require further manipulation before a solution can be found. Here the property of gauge invariance becomes useful: one of the functions g_r, g_θ or g_z can be set arbitrarily without any loss of generality [36]. Choosing $g_r = -g_\theta$ and substituting into the second equation of (15) gives

$$r^2g_r'' + rg_r' - \left[\left(\xi^2 - \frac{\omega^2}{c_2^2}\right)r^2 + (n+1)^2\right]g_r = 0, \tag{16}$$

which is a modified Bessel equation of order $(n+1)$.

Hence solutions for the functions f, g_r, g_θ and g_z can be deduced from Eqs. (15) and (16) in the form of linear combinations of modified Bessel functions as

$$\begin{aligned}f &= AI_n(\alpha r) + BK_n(\alpha r),\\ g_r &= -g_\theta = A_rI_{n+1}(\beta r) + B_rK_{n+1}(\beta r),\\ g_z &= A_zI_n(\beta r) + B_zK_n(\beta r),\end{aligned} \tag{17}$$

where $\alpha^2 = \xi^2 - \omega^2/c_1^2$ and $\beta^2 = \xi^2 - \omega^2/c_2^2$, and I_n and K_n are modified Bessel functions of, respectively, the first and second kinds, of order n. The coefficients A, B, A_r, B_r, A_z and B_z are arbitrary, to be determined from boundary conditions.

The displacements and stresses can be found in terms of the functions given by Eq. (17) by substituting the expressions for the potentials (14) into Eq. (11), recalling that $g_r = -g_\theta$. This gives the displacements as

$$\begin{aligned}u_r &= \left[f' + \frac{n}{r}g_z + i\xi g_r\right]\cos n\theta\, e^{i(\omega t+\xi z)},\\ u_\theta &= \left[-\frac{n}{r}f + i\xi g_r - g_z'\right]\sin n\theta\, e^{i(\omega t+\xi z)},\\ u_z &= \left[i\xi f - \frac{(n+1)}{r}g_r - g_r'\right]\cos n\theta\, e^{i(\omega t+\xi z)}.\end{aligned} \tag{18}$$

The stresses can be determined from Eq. (12) by using the strain definitions (13) with the displacements (18) above. Of the six components of stress, the three which act on cylindrical surfaces of the model (τ_{rr}, $\tau_{r\theta}$ and τ_{rz}) are the most important in the current consideration, because they are involved with the boundary conditions, while the remaining three components ($\tau_{\theta\theta}$, $\tau_{\theta z}$ and τ_{zz}) are internal stresses. The surface stresses are given by

$$\begin{aligned}
\tau_{rr} &= \left[(\lambda+2\mu)f'' + \frac{\lambda}{r}f' - \lambda\left(\frac{n^2}{r^2}+\xi^2\right)f + 2\mu \mathrm{i}\xi g_r' + 2\mu\frac{n}{r}g_z' \right.\\
&\quad \left. -2\mu\frac{n}{r^2}g_z\right]\cos n\theta\, \mathrm{e}^{\mathrm{i}(\omega t+\xi z)},\\
\tau_{r\theta} &= \left[-2\mu\frac{n}{r}f' + 2\mu\frac{n}{r^2}f + \mu \mathrm{i}\xi g_r' - \mu \mathrm{i}\xi\frac{(n+1)}{r}g_r - \mu g_z'' \right.\\
&\quad \left. +\frac{\mu}{r}g_z' - \mu\frac{n^2}{r^2}g_z\right]\sin n\theta\, \mathrm{e}^{\mathrm{i}(\omega t+\xi z)},\\
\tau_{rz} &= \left[2\mu \mathrm{i}\xi f' - \mu g_r'' - \mu\frac{(n+1)}{r}g_r' + \mu\left(\frac{n+1}{r^2}-\xi^2\right)g_r + \mu \mathrm{i}\xi\frac{n}{r}g_z\right]\cos n\theta\, \mathrm{e}^{\mathrm{i}(\omega t+\xi z)},
\end{aligned} \tag{19}$$

and similar expressions can be found for the other three stress components.

The functions f, g_r and g_z are defined in terms of Bessel functions by Eq. (17), while the displacements and stresses are functions of f, g_r and g_z and their derivatives. Thus to determine final expressions for the displacements and stresses, derivatives of Bessel functions must be determined first. The recurrence relations containing derivatives, that is, $I_n'(z) = (n/z)I_n(z) + I_{n+1}(z)$, $K_n'(z) = (n/z)K_n(z) - K_{n+1}(z)$, $I_n'(z) = I_{n-1}(z) - (n/z)I_n(z)$ and $K_n'(z) = -K_{n-1}(z) - (n/z)K_n(z)$ [40], can be used to calculate the required derivatives and thence to find the displacement and stress components of Eqs. (18) and (19) in terms of modified Bessel functions of order n and $(n+1)$. The harmonic solutions can then be written in matrix form as

$$\mathbf{u} = \begin{Bmatrix} u_r \\ u_\theta \\ u_z \end{Bmatrix} = [\mathbf{S}]\cdot[\mathbf{U}]\cdot\mathbf{C}\mathrm{e}^{\mathrm{i}(\omega t+\xi z)},$$

$$\boldsymbol{\tau} = \begin{Bmatrix} \tau_{rr} \\ \tau_{r\theta} \\ \tau_{rz} \\ \tau_{\theta\theta} \\ \tau_{\theta z} \\ \tau_{zz} \end{Bmatrix} = \begin{bmatrix} \mathbf{S} & \mathbf{0} \\ \mathbf{0} & \mathbf{S} \end{bmatrix}\cdot[\mathbf{T}]\cdot\mathbf{C}\mathrm{e}^{\mathrm{i}(\omega t+\xi z)},$$

$$\text{with}\quad [\mathbf{S}] = \begin{bmatrix} \cos n\theta & 0 & 0 \\ 0 & \sin n\theta & 0 \\ 0 & 0 & \cos n\theta \end{bmatrix}. \tag{20}$$

The stress vector has been arranged so that the first three elements are the surface stresses τ_{rr}, $\tau_{r\theta}$ and τ_{rz}. $\mathbf{C} = \{A \quad B \quad A_r \quad B_r \quad A_z \quad B_z\}^{\mathrm{T}}$ is the vector of coefficients, determined from boundary conditions. The 3×6 matrix $[\mathbf{U}]$ defining displacements, and the 6×6 matrix $[\mathbf{T}]$ defining stresses, are given in full in Appendix A.2. The elements of both matrices are in terms of modified Bessel functions with arguments of αr and βr, and thus are functions of wavenumber ξ, frequency ω and circumferential mode number n, as well as radius r and the material properties.

By comparing Eq. (20) to the solutions (4) and (5) for the cylindrical shell, the elastic continuum's displacements and stresses can be written in the wavenumber–frequency domain in a way similar to the shell

result (6). The displacement and surface stress components are

$$\begin{Bmatrix} \tilde{U}_{rn} \\ \tilde{U}_{\theta n} \\ \tilde{U}_{zn} \end{Bmatrix} = [\mathbf{U}] \cdot \mathbf{C} \quad \text{and} \quad \begin{Bmatrix} \tilde{T}_{rrn} \\ \tilde{T}_{r\theta n} \\ \tilde{T}_{rzn} \end{Bmatrix} = [\mathbf{T}_r] \cdot \mathbf{C}, \tag{21}$$

where the 3×6 matrix $[\mathbf{T}_r]$ is the top half of the 6×6 matrix $[\mathbf{T}]$ in Eq. (20).

4. Solution and results for particular boundary conditions

Before the displacements of either the cylindrical shell for the tunnel or the elastic continuum for the soil can be determined, the boundary conditions must be specified. For modelling the tunnel surrounded by soil, the boundary conditions include the applied loads, compatibility of displacements and equilibrium of stresses at the tunnel-soil interface, and a radiation condition for the infinite soil. The equations can of course be used to model the dynamic behaviour of other problems with cylindrical geometry if the appropriate boundary conditions are used, and this provides a means to check the equations before they are used to model the full tunnel-in-soil case.

In general the external loading applied to the tunnel will not be harmonic in space, even if, as here, steady-state harmonic variation in time is of interest. Each general applied stress will instead be a linear combination of the spatially harmonic components given in Eq. (4) for the shell or Eq. (21) for the continuum. The total displacement response can be obtained by using Fourier techniques to add the individual harmonic displacement components which result from each of the harmonic load terms which make up the total load, calculating the components from Eq. (6) or Eq. (21) in combination with the other boundary conditions which apply to a given problem.

4.1. Resolution of a point load

The most useful result for the tunnel model is its response to a unit point load, as the response to a more complicated loading condition can easily be determined by a superposition of point-load cases with suitable translations and rotations. The greatest effect on the tunnel from interaction with a track supported by it is assumed to be via normal reaction forces; the longitudinal and tangential applied forces are therefore set to zero. The spatial variation of such a point load is shown in Fig. 4(a). The response to this load is equivalent to the Green's function of the tunnel for a time-harmonic point load in space.

The problem here is to cast the load into a form which can be utilised with the previously developed results. The cylindrical shell notation will be used for the following argument, but it holds equally for the elastic continuum as well. The loads p_x, p_y and p_z applied to the inside of the shell (which correspond to q_x, q_y and q_z in Eq. (4) if there are no loads applied to the outside of the shell) are stresses. To ensure that the normal stress

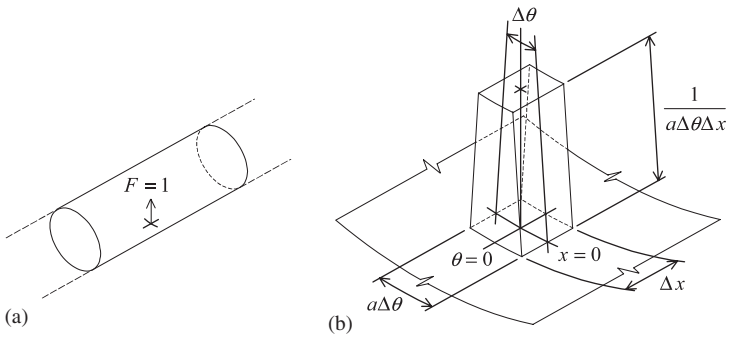

Fig. 4. (a) A unit normal point force acting on the invert of an infinitely long tunnel can be construed as (b) an appropriately scaled uniform normal stress acting over a small rectangular area centred on $x = 0$ and $\theta = 0$. The point force is achieved in the limit as the area tends to zero.

is scaled correctly to be equivalent to a unit force, the spatial variation of the normal loading can be visualised as a 3D rectangular pulse centred on the position $x = 0$ and $\theta = 0$, of small base side-lengths Δx and $a\Delta\theta$, and of height $1/a\Delta\theta\Delta x$, (the stress magnitude), as depicted in Fig. 4(b). The point load is achieved in the limit as Δx and $\Delta\theta$ tend to zero. Thus the state of applied stress for a time-harmonic unit normal point load is

$$p_x = p_y = 0, \quad p_z = \frac{\delta(x)\delta(\theta)}{a} e^{i\omega t}, \tag{22}$$

where $\delta(x)$ and $\delta(\theta)$ are Dirac delta functions.

The solutions for the cylindrical shell (6) and elastic continuum (21) are expressed in the wavenumber-frequency domain for a particular circumferential mode number n. Thus the point load (22) must be decomposed into its space-harmonic components before the displacements can be found. The final displacement results, expressed in the frequency domain as FRFs, will then be linear combinations of the calculated space-harmonic components.

Around the circumference, the space-harmonic variation is represented by the discrete ring modes of order n, while the variation of the load is represented by the term $\delta(\theta)/a$. This part of the load can be written as a linear combination of the ring modes by means of the Fourier cosine series (see Ref. [41])

$$\frac{\delta(\theta)}{a} = \frac{1}{2\pi a} + \sum_{n=1}^{\infty} \frac{1}{\pi a} \cos n\theta \tag{23}$$

on the interval $-\pi < \theta \leqslant \pi$. A Fourier cosine series is used because the Dirac delta function $\delta(\theta)$ is an even function on this interval.

The longitudinal variation of the load is described by the term $\delta(x)$. Since the tunnel is infinitely long, the harmonic components are found by taking the Fourier transform of this term, rather than using discrete modes. Conversely, the total longitudinal variation of the load is described by the inverse Fourier transform of the resulting function $\tilde{\delta}(\xi)$. Thus,

$$\begin{aligned} \tilde{\delta}(\xi) &= \int_{-\infty}^{\infty} \delta(x) e^{-i\xi x} \, dx = 1 \quad \text{for all } \xi \\ \text{and} \quad \delta(x) &= \frac{1}{2\pi} \int_{-\infty}^{\infty} \tilde{\delta}(\xi) e^{i\xi x} \, d\xi = \frac{1}{2\pi} \int_{-\infty}^{\infty} 1 \, e^{i\xi x} \, d\xi, \end{aligned} \tag{24}$$

where the Fourier transform pair used has the factor of $1/2\pi$ in the inverse transform. This definition will prove the most convenient for transformations from the space to wavenumber domain and vice-versa.

Substituting the results for $\delta(\theta)/a$ and $\delta(x)$ from Eqs. (23) and (24) into Eq. (22) yields

$$\begin{aligned} p_x &= p_y = 0, \\ p_z &= \frac{1}{2\pi} \int_{-\infty}^{\infty} \left(\frac{1}{2\pi a} + \frac{1}{\pi a} \sum_{n=1}^{\infty} \cos n\theta \right) e^{i\xi x} \, d\xi \, e^{i\omega t} \end{aligned} \tag{25}$$

for the state of applied stress. Recalling that Eq. (25) is a transform of a sum of modal space-harmonic stress components and comparing it with those components in Eq. (4) allows the harmonic stresses for a particular circumferential mode number n to be deduced as

$$\tilde{P}_{xn} = 0, \quad \tilde{P}_{yn} = 0, \quad \tilde{P}_{zn} = \begin{cases} 1/2\pi a, & n = 0, \\ 1/\pi a, & n \geqslant 0, \end{cases} \tag{26}$$

for all ξ. The harmonic displacements $\{\tilde{U}_n \quad \tilde{V}_n \quad \tilde{W}_n\}^T$ are calculated for each value of n from Eq. (6) by applying the harmonic stresses (26). The total displacements resulting from a time-harmonic unit point load are given by the linear combination of these spatially harmonic components. In the same way as the load, the linear combination is achieved by the inverse Fourier transform of a sum of the modal components, but this time there are no scaling factors explicitly apparent, since the modal displacements are derived from the

correctly scaled modal stresses. Thus the total displacements are given by

$$\begin{Bmatrix} u \\ v \\ w \end{Bmatrix} = \begin{Bmatrix} U \\ V \\ W \end{Bmatrix} e^{i\omega t} = \frac{1}{2\pi}\int_{-\infty}^{\infty} \left(\begin{Bmatrix} \tilde{U}_0 \\ 0 \\ \tilde{W}_0 \end{Bmatrix} + \sum_{n=1}^{\infty} \begin{Bmatrix} \tilde{U}_n \cos n\theta \\ \tilde{V}_n \sin n\theta \\ \tilde{W}_n \cos n\theta \end{Bmatrix} \right) e^{i\xi x}\, d\xi\, e^{i\omega t}, \tag{27}$$

where the term which would correspond to $\tilde{V}_0$ is zero because it is properly multiplied by $\sin n\theta|_{n=0} = 0$, while the other two elements of the same vector are properly multiplied by $\cos n\theta|_{n=0} = 1$. In other words, the total wavenumber-domain displacements $\tilde{U}$ and $\tilde{W}$ are Fourier cosine series, while the displacement $\tilde{V}$ is a Fourier sine series. In practice it is not possible to calculate an infinite number of circumferential modes for the summation, so only as many as required to reach satisfactory convergence are used.

Thus the general time-harmonic displacement response is the inverse Fourier transform of a sum of the circumferential modes in the wavenumber domain. The result (27) holds for any type of time-harmonic loading condition; the modal displacements $\{\tilde{U}_n \quad \tilde{V}_n \quad \tilde{W}_n\}^{\mathrm{T}}$ just have to be calculated for the correct modal stress components, in place of those given by Eq. (26) for the normal point load. More general loads that are *not* harmonic in time could be treated by introducing a second inverse Fourier transform from the frequency to time domain.

4.2. Modelling a thin-walled cylinder with the elastic continuum theory

A useful check on the solutions (6) for the cylindrical shell and (21) for the elastic continuum, and for the validity of using thin-shell theory for the tunnel, is to make use of the continuum theory to model a thin-walled cylinder.

For an infinitely long, free cylindrical shell loaded on the inside surface only, the modal loading components $\tilde{\mathbf{Q}}_n$ of Eq. (4) will simply be the applied loading $\tilde{\mathbf{P}}_n$. Thus the modal displacement components can be calculated from Eq. (6) as

$$\begin{Bmatrix} \tilde{U}_n \\ \tilde{V}_n \\ \tilde{W}_n \end{Bmatrix} = \frac{-a(1-\nu^2)}{Eh}[\mathbf{A}]^{-1} \begin{Bmatrix} \tilde{P}_{xn} \\ \tilde{P}_{yn} \\ \tilde{P}_{zn} \end{Bmatrix}. \tag{28}$$

To obtain an equivalent solution using continuum theory is more complicated. To begin with, the conventional notations used in shell theory and continuum theory do not correspond exactly to one another. The relationships between the displacements and stresses in the two different coordinate systems can be found by comparing Figs. 1 and 3. They are

$$\begin{aligned} u &\equiv u_z, & \tau_{zx} &\equiv -\tau_{rz}, \\ v &\equiv u_\theta, & \tau_{zy} &\equiv -\tau_{r\theta}, \\ w &\equiv -u_r, & \tau_{zz} &\equiv \tau_{rr}, \end{aligned} \tag{29}$$

where the shell quantities have been given first. The shell coordinate system is more convenient here, because in this system stresses applied to an inside cylindrical surface (such as a tunnel invert) are positive in the same direction as the resulting displacements.

The thin-walled cylinder equivalent to the shell will have an inside radius of the mean shell radius *minus* half the shell thickness, and an outside one of the mean radius *plus* half the thickness. The applied stresses on the inside are the same as before, taking note of the differences in directions given by Eq. (29), and the outside ones are again zero. Using Eq. (21), these stress boundary conditions can be written

$$[\mathbf{T}_r]_{r=a-h/2} \cdot \mathbf{C} = \begin{Bmatrix} \tilde{P}_{zn} \\ -\tilde{P}_{yn} \\ -\tilde{P}_{xn} \end{Bmatrix} \quad \text{and} \quad [\mathbf{T}_r]_{r=a+h/2} \cdot \mathbf{C} = \begin{Bmatrix} 0 \\ 0 \\ 0 \end{Bmatrix}, \tag{30}$$

and are sufficient to solve for the 6×1 vector of coefficients $\mathbf{C}$, which can then be substituted into the displacement expression of Eq. (21). For direct comparison to the thin-shell result (28), the displacements should be calculated for the mean radius of the cylinder wall. Thus the modal displacement components are given by

$$\begin{Bmatrix} \tilde{U}_{rn} \\ \tilde{U}_{\theta n} \\ \tilde{U}_{zn} \end{Bmatrix} = [\mathbf{U}]_{r=a} \cdot \begin{bmatrix} [\mathbf{T}_r]_{r=a-h/2} \\ [\mathbf{T}_r]_{r=a+h/2} \end{bmatrix}^{-1} \cdot \begin{Bmatrix} \tilde{P}_{zn} \\ -\tilde{P}_{yn} \\ -\tilde{P}_{xn} \\ 0 \\ 0 \\ 0 \end{Bmatrix}. \tag{31}$$

Either of the solutions (28) or (31) can be used to determine the total displacement due to a particular set of load stresses by a modal summation then inverse Fourier transform, as given by Eq. (27). If the cylinder is excited by a normal point load, then the stress components (26) are used in Eq. (28) or (31).

4.3. Results for the thin-walled cylinder

The numerical results for the thin-walled cylinder were calculated using the unit point load described by Eq. (26) to determine the wavenumber-domain modal displacement components from Eq. (28) for the shell theory, or Eq. (31) for the continuum theory, for a range of modenumber n. These components were then summed and inverse Fourier transformed as in Eq. (27) to give total displacements in the space domain.

The geometry and material parameters were chosen for comparison to match those used by Tuchinda [42], who used the FE method to model a free, infinitely long cylindrical shell. An 88m-long cylindrical unit of 704 8-node thick-shell elements (16 circumferentially by 44 longitudinally) was analysed to compute its dynamic-stiffness matrix. Periodic structure theory was applied to this dynamic-stiffness matrix to join the cylindrical units at 8 nodes at each end, giving the dynamic-stiffness matrix of a semi-infinite cylindrical shell, two of which make an infinite shell.

The numerical values of the parameters used are given in Table 1. Those for the shell theory come directly from values given in Ref. [42], while those for the continuum theory are derived from them. The material parameters are for concrete and the radius and thickness are typical for an underground railway tunnel, so the infinite cylinder with these properties represents a very long, free tunnel with no surrounding soil.

The material damping used for the FE model was Rayleigh (proportional) damping, governed by the two parameters α_R and β_R in Table 1. This form of damping is such that the FE model is represented by

$$[\mathbf{M}]\ddot{\mathbf{x}} + [\mathbf{C}]\dot{\mathbf{x}} + [\mathbf{K}]\mathbf{x} = \mathbf{f}, \quad \text{with} \quad [\mathbf{C}] = \alpha_R[\mathbf{M}] + \beta_R[\mathbf{K}], \tag{32}$$

where $[\mathbf{M}]$ is the mass matrix, $[\mathbf{C}]$ the damping matrix, $[\mathbf{K}]$ the stiffness matrix, $\mathbf{x}$ the vector of nodal displacements and $\mathbf{f}$ the vector of forces applied to the nodes. In the frequency domain with $\mathbf{x} = \mathbf{X}e^{i\omega t}$, this is equivalent to using complex mass and stiffness matrices of the form $[\mathbf{M}]^* = (1 + \alpha_R/i\omega)[\mathbf{M}]$

Table 1
Parameter values used to model a thin-walled cylinder

Cylindrical shell	Elastic continuum
$E = 50 \times 10^9$ Pa	$\lambda = 28.85 \times 10^9$ Pa
$v = 0.3$	$\mu = 19.23 \times 10^9$ Pa
$\rho = 2500\,\text{kg/m}^3$	$\rho = 2500\,\text{kg/m}^3$
$\alpha_R = 10\,\text{s}^{-1}$	$c_1 = 5189\,\text{m/s}$
$\beta_R = 40 \times 10^{-6}\,\text{s}$	$c_2 = 2774\,\text{m/s}$
$a = 3.125\,\text{m}$	$\alpha_R = 10\,\text{s}^{-1}$
$h = 0.25\,\text{m}$	$\beta_R = 40 \times 10^{-6}\,\text{s}$
	r from a and h

and $[\mathbf{K}]^* = (1 + i\omega\beta_R)[\mathbf{K}]$ without a separate damping matrix [**C**]. The Rayleigh damping can thus similarly be accounted for in the continuous shell model (28) by including the mass-proportional damping in a complex density $\rho^* = \rho(1 + \alpha_R/i\omega)$ and the stiffness-proportional damping in a complex Young's modulus $E^* = E(1 + i\omega\beta_R)$. The same complex density can be used in the corresponding elastic-continuum result (31), while Lamé's constants λ and μ are proportional to E and so can be replaced by the complex values $\lambda^* = \lambda(1 + i\omega\beta_R)$ and $\mu^* = \mu(1 + i\omega\beta_R)$. Rayleigh damping is only used here to allow comparison to the FE results. Loss-factor damping as used later is perfectly adequate for most purposes.

Once the modal wavenumber-domain displacements are calculated from Eq. (28) or Eq. (31), the total solution is obtained by substituting them into Eq. (27). This involves two operations: a sum of circumferential modes and an inverse Fourier transform from the ξ- to x-domain. The ξ-domain displacements are calculated numerically by matrix operations on the analytical solutions, so the transform must also be done numerically, using the inverse discrete Fourier transform (DFT). The inverse DFT was calculated using an inverse fast Fourier transform (FFT). As with any use of the DFT, the Nyquist criterion must be met to avoid aliasing and correctly capture all ξ-components. In practice, the DFT can be considered equivalent to the Fourier transform if both the sample and its transform decay to zero at their respective extremities. These issues are discussed further in the thesis [4].

Individual modal displacement components can be transformed into the space domain to check that the Nyquist criterion is satisfied and to examine modal behaviour. Fig. 5 shows the radial modal displacement for $n = 3$ in both the wavenumber and space domains, calculated from the shell theory. The DFT was calculated using a spacing step of $\Delta x = 0.5\,\text{m}$ and a total number of points of $N = 2048$. Fig. 5(a) shows this displacement at a frequency of 30 Hz. The displacement is a sharp localised pulse at $x = 0$ and this follows from the broad wavenumber content shown in the ξ-domain. Thus at this frequency, the small Δx is required to give a maximum wavenumber (2π here) large enough to capture all the broad wavenumber information and ensure the Nyquist criterion is met. Fig. 5(b) shows the displacement at a frequency of 50 Hz. In the x-domain

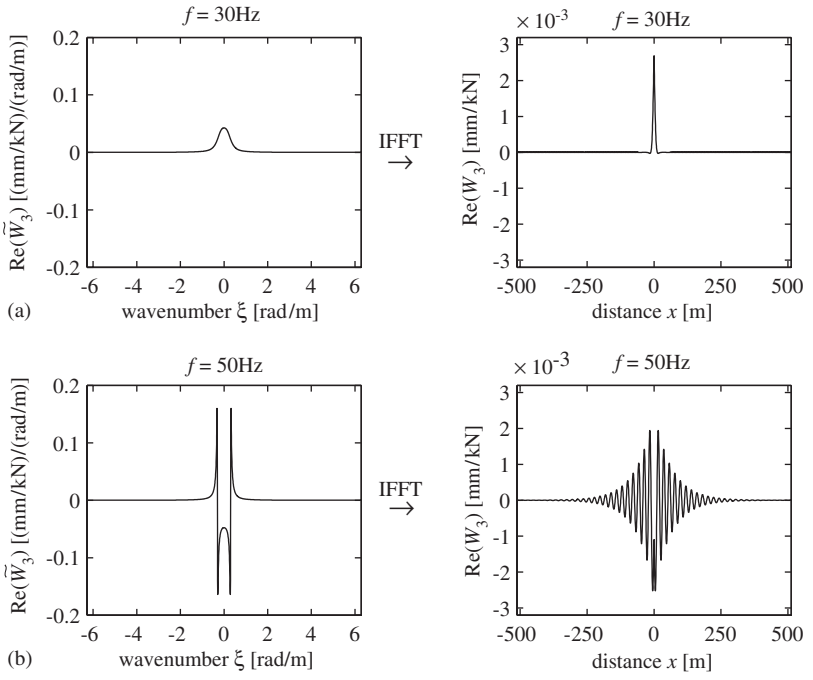

Fig. 5. The real part of the radial modal displacement components $\tilde{W}_n(\xi)$ and $W_n(x)$, for $n = 3$, for an infinitely long, thin cylindrical shell with properties as given in Table 1 and loaded by a unit point force at $x = 0$, at a frequency (a) below the natural frequency for the ring mode and (b) above the natural frequency. The real part in the x-domain represents a "snapshot" for time $t = 0$. The imaginary parts are of similar form. The inverse FFT is done with $\Delta x = 0.5\,\text{m}$ and $N = 2048$ and is performed on the complete complex displacement components $\tilde{W}_n(\xi)$, not just the real parts illustrated. Loading of $\tilde{P}_{xn} = \tilde{P}_{yn} = 0$ and $\tilde{P}_{zn} = 1$.

there is now a propagating wave rather than a localised displacement pulse. In the ξ-domain the displacement is concentrated around a single value of wavenumber of about 0.3 rad/m, corresponding to the 21 m wavelength of the travelling wave. This time the large N is needed to capture all of the displacement response in the x-domain. It can be seen that the chosen values of N and Δx result in all the functions shown in Fig. 5 decaying to zero at the ends of their sample sets, so the inverse DFTs to the x-domain can be trusted as good representations of the actual inverse Fourier transforms.

The transition from localised to propagating modal displacement seen in Fig. 5 occurs at the natural frequency of the $n = 3$ circumferential ring mode. The radial displacement w is associated with in-plane flexural modes of the circular cross-section, Fig. 2(a). The natural frequency f_n of the nth in-plane flexural ring mode for a slender ring is (see Ref. [43])

$$f_n = \frac{1}{2\pi a^2}\frac{n(n^2-1)}{(n^2+1)^{1/2}}\sqrt{\frac{EI_x}{m}} = \frac{1}{2\pi a^2}\frac{n(n^2-1)}{(n^2+1)^{1/2}}\sqrt{\frac{Eh^2}{12\rho}}, \quad n = 1, 2, 3, \ldots \tag{33}$$

where I_x is the second moment of area and m the mass per unit length of the beam forming the circular ring. The right-hand side of Eq. (33) can be applied to the infinitely long thin-walled cylinder. The first in-plane mode associated with w is, however, the expansion mode with $n = 0$. This is really a type of in-plane extensional ring mode, the higher orders of which correspond to tangential displacement v. The natural frequency f_n of the nth in-plane extensional ring mode for a slender ring is [43]

$$f_n = \frac{(1+n^2)^{1/2}}{2\pi a}\sqrt{\frac{E}{\rho}}, \quad n = 0, 1, 2, \ldots . \tag{34}$$

The values of the natural frequencies for the radial in-plane ring modes of the thin-walled cylinder can be calculated from Eqs. (33) and (34) and are given in Table 2 for the first eleven values of n. For the $n = 3$ mode $f_n = 39.9$ Hz, which accords with the localised displacement at 30 Hz and propagating displacement at 50 Hz apparent in Fig. 5.

Having established the spacing and the number of points required for the inverse DFT, there remains the question of how many modal displacement terms have to be included in the Fourier series sum of the solution (27) to give satisfactory convergence. Each modal displacement behaves like the $n = 3$ one discussed above, with a localised displacement below the ring-mode natural frequency, and a propagating displacement above. At a given driving frequency, the response at a point some distance from the driving point will only depend on modal displacements which have begun to propagate, that is, those which have natural frequencies below the driving frequency. From Table 2 it can be deduced that only the modes up to $n = 4$ would have to be included to achieve convergence at a remote point along the cylinder for driving frequencies up to 100 Hz. However, the total driving point response at $x = 0$ has significant contributions from both propagating and localised modal displacements. Nevertheless, the localised modal displacements decrease in maximum magnitude with increasing modenumber n, in other words, the further their natural frequencies lie above the driving frequency. It was found that convergence at $x = 0$, both longitudinally and circumferentially, was reached with a sum of the modes up to $n = 10$ for frequencies up to 100 Hz. Thus all calculations were done using the first eleven modes.

Table 2
Natural frequencies for in-plane ring modes associated with radial displacement of the thin-walled cylinder with properties given in Table 1

n	f_n [Hz]	n	f_n [Hz]
0	227.8	6	181.6
1	0	7	249.9
2	14.1	8	328.8
3	39.9	9	418.2
4	76.5	10	518.2
5	123.8		

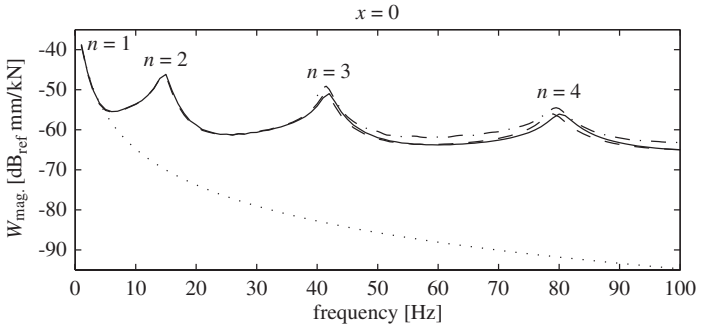

Fig. 6. The radial driving-point response (at $x = 0$, $\theta = 0$) for an infinitely long, free thin-walled cylinder with properties as given in Table 1, showing results calculated from the shell theory ——, continuum theory - - - - and Tuchinda's [42] FE plus periodic-structure approach - · - · -, compared to the driving point response of an infinitely long, free Euler beam ····· with equivalent material and cross-sectional properties. The resonant peaks are marked with their corresponding modenumber n; their frequencies can be compared to those given in Table 2.

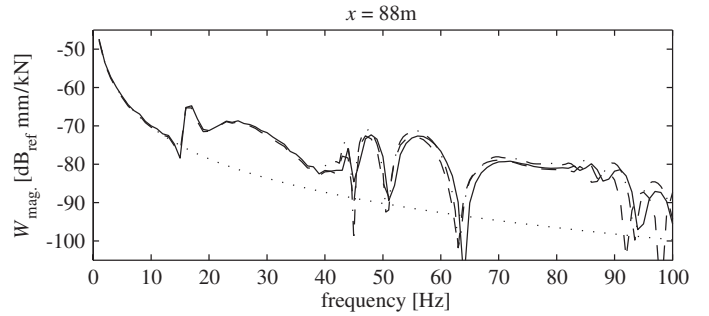

Fig. 7. The radial response of an infinitely long, free cylindrical shell at a point remote ($x = 88$ m, $\theta = 0$) from the normal point load (at $x = 0$, $\theta = 0$), calculated by the same methods and for the same shell properties (Table 1) as Fig. 6: shell ——, continuum - - - -, FE - · - · - and beam ·····.

Fig. 6 gives the driving-point response of the thin-walled cylinder calculated from the shell theory, the continuum theory and from Tuchinda's FE plus periodic-structure method. These three results are also compared to a free bending beam of infinite length, which models the translation of the cross-section ($n = 1$ ring mode) only. Starting from the equation of motion for the bending displacement $y(x, t)$ of an Euler beam (see Ref. [44])

$$m\frac{\partial^2 y}{\partial t^2} + EI\frac{\partial^4 y}{\partial x^4} = f(x,t) \tag{35}$$

loaded by a force distribution per unit length $f(x, t)$, it is straightforward to show that the displacement frequency response $Y(x, \omega)$ of such a beam excited by a unit point harmonic force at $x = 0$ is given by

$$Y(x,\omega) = \frac{1}{4\alpha^3 EI}\left(e^{\alpha|x|} + ie^{i\alpha|x|}\right), \quad \text{with} \quad \alpha^4 = \frac{m\omega^2}{EI}, \tag{36}$$

where m is the mass per unit length of the beam and EI its bending stiffness. The root α used is the second-quadrant one, so that both α and $i\alpha$ have negative real parts and the two exponentials in Eq. (36) decay as $|x| \to \infty$. The beam parameters equivalent to the thin-walled cylinder defined by Table 1 are $m = 12.27 \times 10^3$ kg/m and $EI = 1.200 \times 10^{12}$ Pa m^4.

Fig. 6 shows that the infinite free beam gives a good approximation of the driving-point response until the $n = 2$ ring mode of the cylinder starts to resonate. The resonances correspond well with the calculated ring-mode natural frequencies given in Table 2, but are a little higher because the different types of modes are coupled in the cylinder but not in a ring. Fig. 7 gives the response at 88 m along the infinite cylinder. This time

the bending beam gives a good approximation all the way up to 15 Hz, above which frequency the $n = 2$ ring mode begins propagating from $x = 0$ and reaches $x = 88$ m. Both the driving-point and remote responses show very good agreement between the shell, continuum and FE results. This consistency means firstly that the shell and continuum equations are working correctly and secondly that the use of the shell equations is justified to model the thin-walled cylinder of the tunnel. The tunnel could just as well be modelled by the continuum method, but the shell solution (28) involves one 3×3 matrix instead of the three 3×6 matrices of the continuum solution (31), so saving computation. The shell theory also gives significant savings in computation time and storage requirements over the FE approach, as discussed in the thesis [4].

4.4. Modelling a tunnel in soil

For the complete tunnel-in-soil system, the tunnel is modelled by a cylindrical shell and the soil by an elastic continuum of infinite extent surrounding the tunnel. Three sets of boundary conditions are needed to solve this system completely:

1. The stresses on the inside of the tunnel shell are equal to the applied loading;
2. The displacements must be compatible and the stresses in equilibrium at the interface of the tunnel shell and the soil continuum;
3. The displacements of the soil continuum must decay to zero as the radius from the centre of the tunnel increases towards infinity (the radiation condition).

This time the stresses on the outside of the shell are not zero, so that the first condition can be used with the shell results (6) to write

$$[\mathbf{A}_E] \cdot \tilde{\mathbf{U}}_n = \frac{-Eh}{a(1-\nu^2)}[\mathbf{A}] \begin{Bmatrix} \tilde{U}_n \\ \tilde{V}_n \\ \tilde{W}_n \end{Bmatrix} = \begin{Bmatrix} \tilde{Q}_{xn} \\ \tilde{Q}_{yn} \\ \tilde{Q}_{zn} \end{Bmatrix} = \begin{Bmatrix} \tilde{P}_{xn} \\ \tilde{P}_{yn} \\ \tilde{P}_{zn} \end{Bmatrix} - \begin{Bmatrix} \tilde{T}_{zxn} \\ \tilde{T}_{zyn} \\ \tilde{T}_{zzn} \end{Bmatrix}_{\text{outside}} . \tag{37}$$

The third condition can be used to reduce the dimensions of the equations describing the response of the continuum. It will be recalled that the displacements $\mathbf{u}$ and stresses $\boldsymbol{\tau}$ for the continuum are expressed in Eq. (20) as linear combinations of modified Bessel functions $I_n(\alpha r)$, $K_n(\alpha r)$, $I_n(\beta r)$, $K_n(\beta r)$, $I_{n+1}(\beta r)$ and $K_{n+1}(\beta r)$, originally found as solutions for the functions f, g_r, g_z of Eq. (17) which specify the radial variation of the potentials describing the displacements. It can be shown that, with small loss-factor damping associated with the wavespeeds c_1 and c_2, the principal values of the parameters α and β fall into the first quadrant of the complex plane. For z in this quadrant, $K_n(z)$ tends to zero as $|z| \to \infty$ (see Ref. [45]), whereas $I_n(z)$ increases in magnitude. Thus only the modified Bessel functions of the second kind K_n and K_{n+1} satisfy the radiation condition as $r \to \infty$ and the coefficients of the modified Bessel functions of the first kind I_n and I_{n+1} in Eq. (20) must be set to zero, so that

$$\begin{aligned} A = A_r = A_z = 0 \\ \Rightarrow \mathbf{C} = \{0 \quad B \quad 0 \quad B_r \quad 0 \quad B_z\}^{\mathrm{T}} . \end{aligned} \tag{38}$$

Correspondingly, this means that the terms containing Bessel functions I_n and I_{n+1} in the matrices [**U**] and [**T**] (that is, the first, third and fifth elements of each row) drop out of the equation. Hence the radiation condition reduces the size of the problem for the continuum by half.

The condition of compatibility can be used with the radiation condition expressed by Eq. (38), remembering the differences in the shell and continuum coordinate systems given by Eq. (29), to write the displacements at the tunnel-soil interface as

$$\begin{Bmatrix} \tilde{U}_n \\ \tilde{V}_n \\ \tilde{W}_n \end{Bmatrix} = \begin{Bmatrix} \tilde{U}_{zn} \\ \tilde{U}_{\theta n} \\ -\tilde{U}_{rn} \end{Bmatrix}_{r=a} = \begin{bmatrix} u_{32} & u_{34} & u_{36} \\ u_{22} & u_{24} & u_{26} \\ -u_{12} & -u_{14} & -u_{16} \end{bmatrix}_{r=a} \begin{Bmatrix} B \\ B_r \\ B_z \end{Bmatrix} = [\mathbf{U}_\infty]_{r=a} \cdot \mathbf{B}, \tag{39}$$

while equilibrium means that the stresses at the interface are given by

$$\left\{\begin{array}{c}\tilde{T}_{zxn}\\ \tilde{T}_{zyn}\\ \tilde{T}_{zzn}\end{array}\right\}_{\text{outside}} = \left\{\begin{array}{c}-\tilde{T}_{rzn}\\ -\tilde{T}_{r\theta n}\\ \tilde{T}_{rrn}\end{array}\right\}_{r=a} = \left[\begin{array}{ccc}-t_{32} & -t_{34} & -t_{36}\\ -t_{22} & -t_{24} & -t_{26}\\ t_{12} & t_{14} & t_{16}\end{array}\right]_{r=a} \left\{\begin{array}{c}B\\ B_r\\ B_z\end{array}\right\} = [\mathbf{T}_\infty]_{r=a}\cdot\mathbf{B}, \tag{40}$$

where the u_{jk} and t_{jk} are the remaining elements of $[\mathbf{U}]$ and $[\mathbf{T}_r]$ of Eq. (21). By substituting Eq. (40) into Eq. (37) to eliminate the stresses acting on the outside of the shell tunnel and using Eq. (39), the unknown displacements and coefficients can be found, after some rearrangement, from

$$\left\{\begin{array}{c}\tilde{\mathbf{U}}_n\\ \mathbf{B}\end{array}\right\} = \left[\begin{array}{cc}[\mathbf{A}_E] & [\mathbf{T}_\infty]_{r=a}\\ [\mathbf{I}] & -[\mathbf{U}_\infty]_{r=a}\end{array}\right]^{-1} \left\{\begin{array}{c}\tilde{\mathbf{P}}_n\\ \mathbf{0}\end{array}\right\}, \tag{41}$$

where $[\mathbf{I}]$ is a 3×3 identity matrix. The displacements $\tilde{\mathbf{U}}_n = \{\tilde{U}_n \quad \tilde{V}_n \quad \tilde{W}_n\}^{\mathrm{T}}$ at the interface result directly from Eq. (41), but the displacements at some radius R elsewhere in the soil have to be calculated using the coefficients $\mathbf{B}$ from

$$\tilde{\mathbf{U}}_n|_{r=R} = [\mathbf{U}_\infty]_{r=R}\cdot\mathbf{B}. \tag{42}$$

Of course, the foregoing argument determines the modal displacement components in the wavenumber domain. Once a sufficient number of these have been obtained, Eq. (27) can be used to obtain the total displacements in the space domain.

4.5. Results for the tunnel in soil

Table 3 gives the parameter values used to model the tunnel surrounded by soil. Parameters not used directly in each particular theory (shell or continuum) are nevertheless given to allow direct comparison between the properties of the tunnel and those of the soil. Frequencies up to 200 Hz are of interest for ground-vibration propagation here.

The tunnel parameters are for concrete. The material damping of the concrete is assumed to be negligible compared to that of the soil, so is taken as zero. The tunnel is the same as the thin-walled cylinder described by Table 1, except for a slightly smaller radius and zero damping. The soil parameters fall within the range of those given by Hunt [46] for Oxford Clay and Middle Chalk, and thus represent a nominal constant-volume type soil (Poisson's ratio close to 0.5) for the purposes of demonstrating the use of the model. As in Ref. [46], all energy dissipation due to material damping in the soil is assumed to occur through shear motion, characterised by the shear modulus G, with no losses in volumetric expansion, characterised by the bulk modulus $K = E/3(1-2\nu)$. The constant hysteretic loss factor η_G is derived from the frequency-dependent viscous damping factor in Ref. [46] at 100 Hz. The soil damping is included in the model by using the complex material parameters $G^* = G(1+\mathrm{i}\eta_G)$ and $K^* = K(1+\mathrm{i}\eta_K) = K$ in the frequency domain. Of course, this

Table 3
Parameter values used to model a tunnel surrounded by soil

Tunnel (cylindrical shell)	Soil (elastic continuum)
$E = 50\times 10^9$ Pa	$E = 550\times 10^6$ Pa
$\nu = 0.3$	$\nu = 0.44$
$\rho = 2500$ kg/m^3	$\rho = 2000$ kg/m^3
$c_1 = 5189$ m/s	$\lambda = 1.400\times 10^9$ Pa
$c_2 = 2774$ m/s	$\mu = G = 191\times 10^6$ Pa
$a = 3.0$ m	$K = 1.528\times 10^9$ Pa
$h = 0.25$ m	$c_1 = 944$ m/s
Zero damping	$c_2 = 309$ m/s
	$\eta_G = 0.06$
	$\eta_K = 0$

formulation allows for non-zero volumetric damping η_K if required, as in saturated or nearly saturated soils where viscous losses arising from flow induced by volumetric deformations are important (see, for example, Ref. [47]). In general, damping could be introduced into any two of the elastic parameters and/or the density, and can be an arbitrary function of frequency in each case. For the present damping assumption, the other damped Lamé constant λ^* required can most simply be obtained via the elastic relations and a complex Poisson's ratio ν^*. Although the normal practice is to take ν as the purely real parameter, there is no good reason why this has to be so. A complex Poisson's ratio merely implies a phase difference between the transverse and axial strains in a piece of the material subjected to uniaxial harmonic loading. Thus $\nu^* = \frac{1}{2}(3K^* - 2G^*)/(3K^* + G^*)$, $\mu^* = G^*$ and $\lambda^* = 2G^*\nu^*/(1 - 2\nu^*)$.

Calculation of the total tunnel and soil displacements was done with a sum of modal displacement components and an inverse DFT in the same way described in Section 4.3 for the thin-walled cylinder. However, the modal displacements now depend on Eq. (41) the tunnel ones directly and the soil ones via the coefficients **B** and Eq. (42). The inverse matrix in Eq. (41) comprises four submatrices of vastly different orders of magnitude: the elements of $[\mathbf{A}_E]$ are typically of order 10^{11}, those of $[\mathbf{T}_\infty]_{r=a}$ of order 10^1, those of $[\mathbf{I}]$ of order 10^0 and those of $[\mathbf{U}_\infty]_{r=a}$ of order 10^{-7}, for the parameters of Table 3 and for frequencies up to 200 Hz. This span of 18 orders of magnitude means the assembled matrix is so badly scaled that a numerical solution to Eq. (41) is inaccurate or even impossible. Row and column normalisation was therefore used to reduce the elements of the assembled matrix to magnitudes between zero and unity, before numerical solution. The reciprocal condition-estimator for the matrix in Eq. (41) is typically of the order of 10^{-21} (which is singular to working precision) before any normalisation, 10^{-11} after either row or column normalisation alone, and 10^{-3} after both row and column normalisation, where values near 1.0 indicate well-conditioned matrices.

As for the thin-walled cylinder, the inverse DFT was calculated by FFT, using $N = 2048$ and $\Delta x = 0.5$ m. As before, the individual modal displacements can be checked for sufficient decay at their extremities in both wavenumber and space domains. Both the tunnel and soil displacements were found to satisfy this decay requirement with these values of N and Δx. The tunnel displacement decay with x is particularly rapid compared to the free cylinder case, because the presence of the infinite soil allows energy to propagate away from the tunnel, resulting in a "radiation damping" effect.

A useful feature of the displacements is their symmetry. Because the two halves of the tunnel either side of $x = 0$ are identical, a radial load applied at $x = 0$ as here produces displacements which are mirrored in the $x = 0$ plane. Component U is parallel to the x-axis, so is an odd function of x, while V and W are orthogonal to the x-axis, so are even functions of x. The same is true of the displacement components in the wavenumber domain. This symmetry is useful in the computation of the individual modal displacements, since only values for positive ξ need to be calculated, as the values for negative ξ can be generated by the correct reflection when needed at the inverse DFT stage. Calculating only half the values halves the computation time and disk storage space required, and reduces the amount of memory needed to hold modal components during the summation stage.

The modal displacement components were calculated from Eqs. (41) and (42), summed and then transformed using the inverse FFT to give the total displacements of the tunnel or the soil by Eq. (27). As for the free tunnel, modal displacements from $n = 0$ to $n = 10$ were found to give sufficient convergence for frequencies from 1 to 200 Hz with the model parameters of Table 3. Fig. 8 illustrates the types of responses which can be calculated. It is convenient to look at responses at $\theta = 0$ in the tunnel (corresponding to the tunnel invert upon which a track rests), and responses at $\theta = 90^\circ$ in the soil (corresponding to the horizontal plane likely to contain building foundations), as in both cases the cylindrical coordinate system then coincides with the absolute horizontal, vertical and longitudinal directions. Because of the symmetry about $x = 0$ and $\theta = 0$, some displacements are zero at some of the positions shown. However, all non-zero displacements include the effects of several modal contributions. The tunnel-invert displacements U and W at (ii) are simple sums of all their modal contributions, because $\cos n\theta = 1$ for all n when $\theta = 0$; while at (iv) with $\theta = 90^\circ$, the soil displacements U and W include only the even-numbered modal contributions as $\cos(2k + 1)\theta = 0$ for odd $n = 2k + 1$, and V includes only the odd-numbered modal contributions as $\sin 2k\theta = 0$ for even $n = 2k$.

Fig. 9 shows the driving-point response of the tunnel invert. Only the vertical displacement W is non-zero. This does not show any ring-mode resonances like the free thin-walled cylinder's driving-point response in

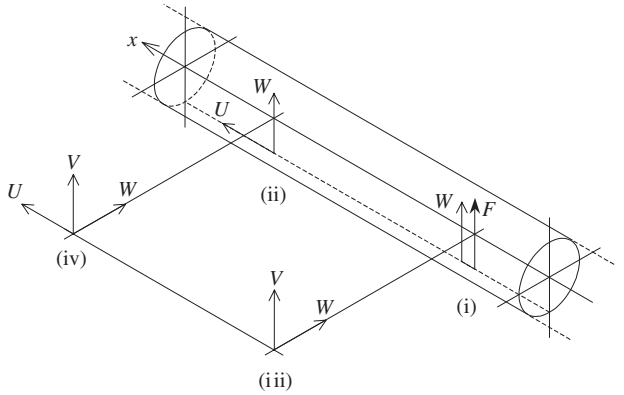

Fig. 8. The non-zero displacement components of the tunnel-in-soil model (i) at the driving point ($x = 0$, $r = 3\,\text{m}$, $\theta = 0$) on the tunnel invert, (ii) at a point on the tunnel invert ($x = 20\,\text{m}$, $r = 3\,\text{m}$, $\theta = 0$) away from the load, (iii) at a point a distance horizontally ($x = 0$, $r = 20\,\text{m}$, $\theta = 90^\circ$) out into the soil, opposite the load, and (iv) at a distance horizontally out into the soil and a distance longitudinally parallel to the tunnel ($x = 20\,\text{m}$, $r = 20\,\text{m}$, $\theta = 90^\circ$).

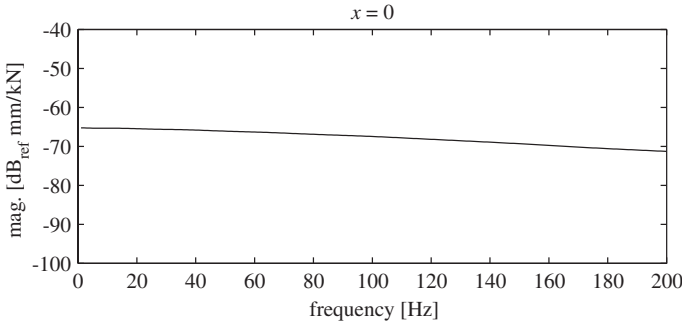

Fig. 9. The vertical driving-point response W of the tunnel in the tunnel-in-soil model with parameters given in Table 3, under a normal unit point force, corresponding to position (i) in Fig. 8. The longitudinal component U is zero because $x = 0$, while the horizontal (tangential) component V is zero because $\theta = 0$.

Fig. 6, but is instead smooth and decreases slightly in magnitude as frequency increases. The loss of noticeable resonances is due to the radiation damping of the infinite soil now surrounding the tunnel.

Fig. 10 shows the response of the tunnel invert at a distance of 20 m from the load. The vertical response W has troughs at about 51, 119 and 184 Hz. The spacing between these is 68 and 65 Hz, respectively. This regular frequency spacing suggests some kind of correspondence of wavelength with distance from the load to the observation point. In interference patterns, the condition for a point at a fixed distance L from a source to be a node at successive frequencies is that an extra half wavelength must be fitted within that distance each time. Given a wavespeed of c, this extra half wavelength results in a frequency step of $c/2L$ between successive interference patterns that fit the distance. For a distance of 20 m, the speed of shear (transverse) waves in the tunnel concrete of $c_2 = 2774\,\text{m/s}$ gives a frequency step of 69 Hz, which matches the observed spacing between the troughs in the vertical (transverse) displacement W. The longitudinal displacement U exhibits less pronounced variation, with changing frequency intervals between troughs, none of which seem to correspond to the shear- or pressure-wave speeds in either the tunnel concrete or the soil. The variation is probably due to the behaviour of the interface between the tunnel and the soil.

Fig. 11 shows the response of the tunnel invert at 30 m, a little further from the load than for Fig. 10. Again, there are regularly spaced troughs in the vertical displacement W. Above 60 Hz, there exist dips at about 62, 111, 159 Hz and somewhere at or above 200 Hz. The first three of these give frequency steps of 49 and 48 Hz, while the concrete shear-wave speed of $c_2 = 2774\,\text{m/s}$ again gives a closely matching step of 46 Hz for a distance of 30 m. There therefore appears to be a strong relationship between the tunnel's radial response and

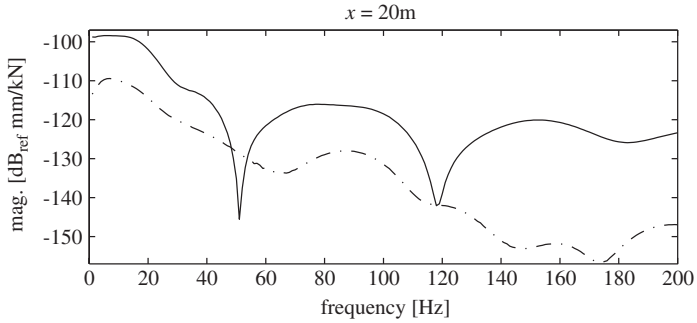

Fig. 10. The response of the tunnel invert at a distance $x = 20$ m from the load, corresponding to position (ii) in Fig. 8, for tunnel-in-soil parameters given in Table 3, showing the vertical component W —— and the longitudinal component U - - - - -. The horizontal (tangential) component V is zero because $\theta = 0$.

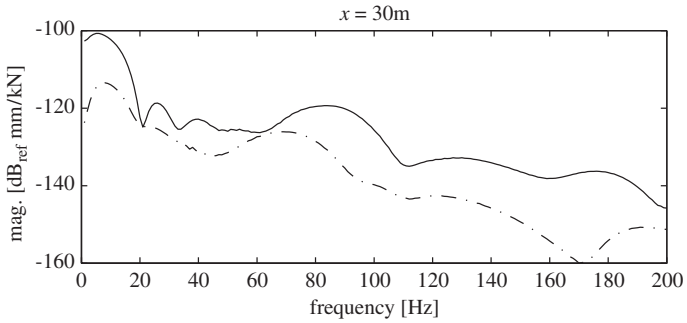

Fig. 11. The response of the tunnel invert at a distance $x = 30$ m from the load, corresponding to position (ii) in Fig. 8 shifted further down the tunnel, for tunnel-in-soil parameters given in Table 3, showing the vertical component W —— and the longitudinal component U - - - - -. The horizontal (tangential) component V is zero because $\theta = 0$.

the propagation of shear waves in the tunnel wall. Interestingly, at lower frequency, three dips in W at about 21, 34 and 47 Hz give a frequency step of 13 Hz, which is close to the 16 Hz calculated for 30m distance using the soil's pressure-wave speed $c_1 = 944$ m/s. The longitudinal displacement U is again more ambiguous. While at first it may seem impossible for a single source to create interference patterns in an infinite system, a consideration of the geometry can provide a possible explanation. For waves confined to the tunnel shell or the tunnel-soil interface, there are at least two different path lengths from the load to a fixed point on the tunnel wall. This is due to the closed nature of the cylindrical shell (indeed, it is this which gives rise to the ring modes). For the arrangement considered here, there is the direct longitudinal path along the tunnel floor, and a less direct helical path of one turn around the cylindrical surface. Clearly, there is a complex interaction of propagation, interference and radiation effects contributing to the tunnel's overall response.

Fig. 12 shows the soil response 20 m horizontally opposite the position of the load applied to the tunnel. The horizontal displacement W shows clear undulations with a step of about 20 Hz between troughs (or peaks), while the vertical displacement V shows similar, but very slight, undulation. This is probably due to interference effects, with points along the tunnel acting as sources transmitting energy propagated from the load. At each "source", some energy radiates into the soil and the remainder continues along the tunnel. The exact distribution of "sources" will depend on which parts of the tunnel show maximum activity at a given frequency. However, the load at $x = 0$ will always act as one of the sources. Thus the distance between the load and the observation point can be used to estimate the frequency step between the peaks or the troughs in Fig. 12. As explained above, the frequency step between successive interference patterns that fit the distance is $c/2L$. The direct distance from the bottom of the tunnel (of radius 3 m), where the load is applied, to the point 20 m horizontally out into the soil, is 20.2 m, although this line cuts through the tunnel cross-section. For a distance L of 20.2 m, soil pressure waves of speed $c_1 = 944$ m/s give a frequency step of 23.3 Hz, while shear

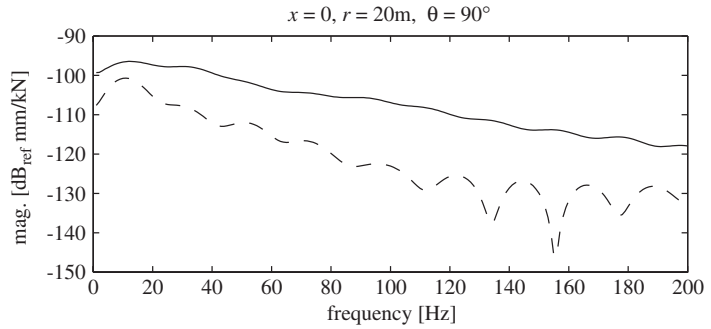

Fig. 12. The response in the soil at $x = 0$, $r = 20\,\text{m}$, $\theta = 90^\circ$, horizontally opposite the point load acting on the tunnel invert, corresponding to position (iii) in Fig. 8, for tunnel-in-soil parameters given in Table 3, showing the vertical component V —— and the horizontal component W - - - -. The longitudinal component U is zero because $x = 0$.

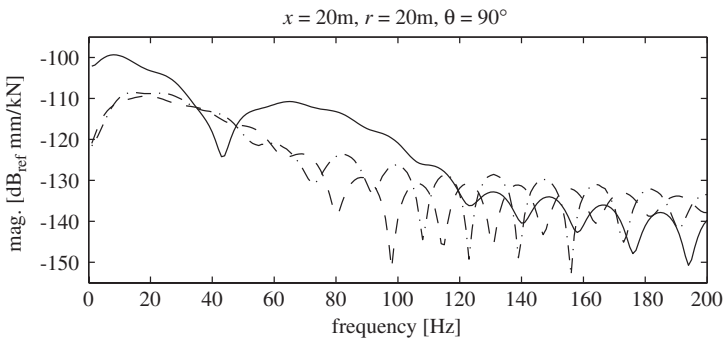

Fig. 13. The response in the soil at $x = 20\,\text{m}$, $r = 20\,\text{m}$, $\theta = 90^\circ$, horizontally out from the load then parallel to the tunnel, corresponding to position (iv) in Fig. 8, for tunnel-in-soil parameters given in Table 3, showing the vertical component V ——, the horizontal component W - - - - and the longitudinal component U - · - · -.

waves of speed $c_2 = 309\,\text{m/s}$ give a step of 7.6 Hz. Thus the undulating response of Fig. 12 appears to be due to the interference of pressure waves propagating through the soil from different points along the tunnel. Hence the greatest influence is on W, which lies nearly along the line of propagation which is also the direction of oscillation of the pressure (longitudinal) waves; there is little influence on V, which lies nearly perpendicular to the line of propagation.

The dominance of pressure-wave effects in the soil in this case raises the question of the influence of shear waves. The answer lies in the material damping. Reduction in magnitude due to material damping depends on the number of cycles of vibration the material has gone through: the more cycles, the more reduction. Since the speed of pressure waves in the soil is about three times the speed of shear waves, a propagating shear wave will go through three times as many cycles as a propagating pressure wave over the same distance, for any given frequency. If the reduction per cycle due to material damping were the same for all types of motion, then it would be expected that shear-wave magnitudes would be reduced by the cube of the factor that pressure-wave magnitudes are. However, the original assumption was that all material damping losses in the soil are due to shear motion. Therefore material damping has a much bigger effect here on the decay of shear waves than of pressure waves, even without considering number of cycles, and after some distance of propagation, pressure waves are predominant.

Fig. 13 shows the response of the soil at a radius of 20 m horizontally from the centre of the tunnel and 20 m longitudinally from the load on the invert. This means the observation point is a direct distance of 28.4 m from the load. This distance gives a frequency step of 16.6 Hz for pressure waves involved in interference. Undulations of about this spacing can be clearly seen in the horizontal and longitudinal displacements W and U (each with a significant component in the direction of the line of propagation) above 60 Hz, and in the vertical displacement V (which is nearer orthogonal to the line of propagation) above 120 Hz. On a larger

scale, dips in V can be observed at 43 and 123 Hz. These correspond quite closely to the vertical displacement of the tunnel invert at 20 m from the load (Fig. 10), the part of the tunnel closest to the soil observation point here. In the case of V, the adjacent vertical tunnel displacement is transmitted by shear waves. Above 120 Hz, the shear waves complete eight or more cycles over 20 m, so have decayed sufficiently that the pressure-wave effects appear clearly in V. Thus it appears that at lower frequencies the local displacement of the tunnel has the biggest effect on the soil displacement, while at higher frequencies interference effects dominate.

5. Conclusions

A tunnel surrounded by soil can be modelled by considering the tunnel as an infinitely long, thin cylindrical shell and the soil as an infinite homogeneous isotropic continuum. An analytical solution for the time-harmonic displacements of the tunnel and soil can be found in the form of the spatial inverse Fourier transform of an infinite sum of components, representing ring modes of the tunnel cross-section, which are harmonic in both space and time. The modal harmonic displacement components are calculated from the modal harmonic components of the total load applied to the tunnel. Numerical computation of results from this analytical solution is straightforward for typical values of tunnel and soil parameters. The infinite sum converges with the first eleven terms, and the inverse Fourier transform is satisfactorily represented by an inverse DFT of 2048 sample points, of which symmetry requires only 1025 to be calculated. The computation time and disk storage space required for the analytical solution are much more modest than those for an FE model of the same system.

Numerical results for the case of a normal unit point load applied to the tunnel invert reveal several aspects of the system's behaviour. A tunnel surrounded by soil does not show the ring-mode resonances apparent in the driving-point response of a free tunnel, due to the radiation-damping effect of the infinite soil. For the parameter set considered in this paper, the response of the tunnel away from the load is influenced by the propagation of shear waves in the tunnel material and interaction with the soil interface. The soil response seems to be influenced in large measure by the response of the closest part of the tunnel, with strong interference patterns based on soil pressure waves propagating from different parts of the tunnel appearing particularly in the higher part of the frequency range, where shear-wave effects are reduced by soil damping. The tunnel-in-soil model can be used as a realistic track foundation so that the true effectiveness of floating-slab track can be evaluated by looking at soil responses directly. This latter subject is explored in the companion paper [1].

Acknowledgement

The work described in this paper was undertaken while the first author was a doctoral candidate at the University of Cambridge supported by a Cambridge Commonwealth Trust scholarship and an Overseas Research Students award.

Appendix A. Shell and continuum coefficients

A.1. Coefficients for the cylindrical shell

The elements of the matrix [**A**] used in Eq. (6) to calculate the displacements of the cylindrical shell are given below. These coefficients are derived from the Flügge shell equations.

$$a_{11} = \frac{\rho a(1-\nu^2)}{E}\omega^2 - a\xi^2 - \frac{(1-\nu)}{2a}\left(1+\frac{h^2}{12a^2}\right)n^2,$$

$$a_{12} = \frac{(1+\nu)}{2}\mathrm{i}\xi n,$$

$$a_{13} = -\nu \mathrm{i}\xi + \frac{h^2}{12}(\mathrm{i}\xi)^3 + \frac{h^2}{12a^2}\frac{(1-\nu)}{2}\mathrm{i}\xi n^2,$$

$$a_{21} = -\frac{(1+\nu)}{2}\mathrm{i}\xi n,$$

$$a_{22} = \frac{\rho a(1-\nu^2)}{E}\omega^2 - \frac{a(1-\nu)}{2}\left(1 + \frac{h^2}{4a^2}\right)\xi^2 - \frac{1}{a}n^2,$$

$$a_{23} = \frac{1}{a}n + \frac{h^2}{12}\frac{(3-\nu)}{2a}\xi^2 n,$$

$$a_{31} = \nu \mathrm{i}\xi - \frac{h^2}{12}(\mathrm{i}\xi)^3 - \frac{h^2}{12a^2}\frac{(1-\nu)}{2}\mathrm{i}\xi n^2,$$

$$a_{32} = \frac{1}{a}n + \frac{h^2}{12a}\frac{(3-\nu)}{2}\xi^2 n,$$

$$a_{33} = \frac{\rho a(1-\nu^2)}{E}\omega^2 - \frac{h^2}{12}\left(a\xi^4 + \frac{2}{a}\xi^2 n^2 + \frac{1}{a^3}n^4\right) - \frac{1}{a} + \frac{h^2}{12a^3}\left(2n^2 - 1\right).$$

A.2. Coefficients for the elastic continuum

The elements of the matrix [**U**] used to determine the displacement components of the continuum in Eq. (20) are:

$$u_{11} = \frac{n}{r}I_n(\alpha r) + \alpha I_{n+1}(\alpha r),$$

$$u_{12} = \frac{n}{r}K_n(\alpha r) - \alpha K_{n+1}(\alpha r),$$

$$u_{13} = \mathrm{i}\xi I_{n+1}(\beta r),$$

$$u_{14} = \mathrm{i}\xi K_{n+1}(\beta r),$$

$$u_{15} = \frac{n}{r}I_n(\beta r),$$

$$u_{16} = \frac{n}{r}K_n(\beta r),$$

$$u_{21} = -\frac{n}{r}I_n(\alpha r),$$

$$u_{22} = -\frac{n}{r}K_n(\alpha r),$$

$$u_{23} = \mathrm{i}\xi I_{n+1}(\beta r),$$

$$u_{24} = \mathrm{i}\xi K_{n+1}(\beta r),$$

$$u_{25} = -\frac{n}{r}I_n(\beta r) - \beta I_{n+1}(\beta r),$$

$$u_{26} = -\frac{n}{r}K_n(\beta r) + \beta K_{n+1}(\beta r),$$

$$u_{31} = \mathrm{i}\xi I_n(\alpha r),$$

$$u_{32} = \mathrm{i}\xi K_n(\alpha r),$$

$$u_{33} = -\beta I_n(\beta r),$$

$$u_{34} = \beta K_n(\beta r),$$

$$u_{35} = 0,$$

$$u_{36} = 0.$$

The elements of the matrix [**T**] used to determine the stress components of the continuum in Eq. (20) are:

$$t_{11} = \left(2\mu\frac{(n^2-n)}{r^2} - \lambda\xi^2 + (\lambda+2\mu)\alpha^2\right)I_n(\alpha r) - 2\mu\frac{\alpha}{r}I_{n+1}(\alpha r),$$

$$t_{12} = \left(2\mu\frac{(n^2-n)}{r^2} - \lambda\xi^2 + (\lambda+2\mu)\alpha^2\right)K_n(\alpha r) + 2\mu\frac{\alpha}{r}K_{n+1}(\alpha r),$$

$$t_{13} = 2\mu\mathrm{i}\xi\beta I_n(\beta r) - 2\mu\mathrm{i}\xi\frac{(n+1)}{r}I_{n+1}(\beta r),$$

$$t_{14} = -2\mu\mathrm{i}\xi\beta K_n(\beta r) - 2\mu\mathrm{i}\xi\frac{(n+1)}{r}K_{n+1}(\beta r),$$

$$t_{15} = 2\mu\frac{(n^2-n)}{r^2}I_n(\beta r) + 2\mu\frac{n}{r}\beta I_{n+1}(\beta r),$$

$$t_{16} = 2\mu\frac{(n^2-n)}{r^2}K_n(\beta r) - 2\mu\frac{n}{r}\beta K_{n+1}(\beta r),$$

$$t_{21} = -2\mu\frac{(n^2-n)}{r^2}I_n(\alpha r) - 2\mu\frac{n}{r}\alpha I_{n+1}(\alpha r),$$

$$t_{22} = -2\mu\frac{(n^2-n)}{r^2}K_n(\alpha r) + 2\mu\frac{n}{r}\alpha K_{n+1}(\alpha r),$$

$$t_{23} = \mu\mathrm{i}\xi\beta I_n(\beta r) - 2\mu\mathrm{i}\xi\frac{(n+1)}{r}I_{n+1}(\beta r),$$

$$t_{24} = -\mu\mathrm{i}\xi\beta K_n(\beta r) - 2\mu\mathrm{i}\xi\frac{(n+1)}{r}K_{n+1}(\beta r),$$

$$t_{25} = \left(-2\mu\frac{(n^2-n)}{r^2} - \mu\beta^2\right)I_n(\beta r) + 2\mu\frac{\beta}{r}I_{n+1}(\beta r),$$

$$t_{26} = \left(-2\mu\frac{(n^2-n)}{r^2} - \mu\beta^2\right)K_n(\beta r) - 2\mu\frac{\beta}{r}K_{n+1}(\beta r),$$

$$t_{31} = 2\mu\mathrm{i}\xi\frac{n}{r}I_n(\alpha r) + 2\mu\mathrm{i}\xi\alpha I_{n+1}(\alpha r),$$

$$t_{32} = 2\mu\mathrm{i}\xi\frac{n}{r}K_n(\alpha r) - 2\mu\mathrm{i}\xi\alpha K_{n+1}(\alpha r),$$

$$t_{33} = -\mu\frac{n}{r}\beta I_n(\beta r) - \mu(\xi^2+\beta^2)I_{n+1}(\beta r),$$

$$t_{34} = \mu\frac{n}{r}\beta K_n(\beta r) - \mu(\xi^2 + \beta^2)K_{n+1}(\beta r),$$

$$t_{35} = \mu \mathrm{i}\xi\frac{n}{r}I_n(\beta r),$$

$$t_{36} = \mu \mathrm{i}\xi\frac{n}{r}K_n(\beta r),$$

$$t_{41} = \left(-2\mu\frac{(n^2-n)}{r^2} + \lambda(\alpha^2 - \xi^2)\right)I_n(\alpha r) + 2\mu\frac{\alpha}{r}I_{n+1}(\alpha r),$$

$$t_{42} = \left(-2\mu\frac{(n^2-n)}{r^2} + \lambda(\alpha^2 - \xi^2)\right)K_n(\alpha r) - 2\mu\frac{\alpha}{r}K_{n+1}(\alpha r),$$

$$t_{43} = 2\mu \mathrm{i}\xi\frac{(n+1)}{r}I_{n+1}(\beta r),$$

$$t_{44} = 2\mu \mathrm{i}\xi\frac{(n+1)}{r}K_{n+1}(\beta r),$$

$$t_{45} = -2\mu\frac{(n^2-n)}{r^2}I_n(\beta r) - 2\mu\frac{n}{r}\beta I_{n+1}(\beta r),$$

$$t_{46} = -2\mu\frac{(n^2-n)}{r^2}K_n(\beta r) + 2\mu\frac{n}{r}\beta K_{n+1}(\beta r),$$

$$t_{51} = -2\mu \mathrm{i}\xi\frac{n}{r}I_n(\alpha r),$$

$$t_{52} = -2\mu \mathrm{i}\xi\frac{n}{r}K_n(\alpha r),$$

$$t_{53} = \mu\frac{n}{r}\beta I_n(\beta r) - \mu\xi^2 I_{n+1}(\beta r),$$

$$t_{54} = -\mu\frac{n}{r}\beta K_n(\beta r) - \mu\xi^2 K_{n+1}(\beta r),$$

$$t_{55} = -\mu \mathrm{i}\xi\frac{n}{r}I_n(\beta r) - \mu \mathrm{i}\xi\beta I_{n+1}(\beta r),$$

$$t_{56} = -\mu \mathrm{i}\xi\frac{n}{r}K_n(\beta r) + \mu \mathrm{i}\xi\beta K_{n+1}(\beta r),$$

$$t_{61} = \left(\lambda\alpha^2 - (\lambda + 2\mu)\xi^2\right)I_n(\alpha r),$$

$$t_{62} = \left(\lambda\alpha^2 - (\lambda + 2\mu)\xi^2\right)K_n(\alpha r),$$

$$t_{63} = -2\mu \mathrm{i}\xi\beta I_n(\beta r),$$

$$t_{64} = 2\mu \mathrm{i}\xi\beta K_n(\beta r),$$

$$t_{65} = 0,$$

$$t_{66} = 0.$$

References

[1] J.A. Forrest, H.E.M. Hunt, Ground vibration generated by trains in underground tunnels, *Journal of Sound and Vibration* this issue, (2005) 10.1016/j.jsv.2005.12.031.

[2] R.J. Greer, C.J. Manning, Vibration isolation for railways, *Acoustics Bulletin* 23 (1998) 13–17.

[3] M. Heckl, G. Hauck, R. Wettschureck, Structure-borne sound and vibration from rail traffic, *Journal of Sound and Vibration* 193 (1996) 175–184.

[4] J.A. Forrest, Modelling of Ground Vibration from Underground Railways, PhD Thesis, University of Cambridge, 1999.

[5] R.A. Hood, R.J. Greer, M. Breslin, P.R. Williams, The calculation and assessment of ground-borne noise and perceptible vibration from trains in tunnels, *Journal of Sound and Vibration* 193 (1996) 215–225.

[6] S. Kraemer, Noise and Vibration in Buildings from Underground Railway Lines, PhD Thesis, University of London, 1984.

[7] J. Melke, Noise and vibration from underground railway lines: proposals for a prediction procedure, *Journal of Sound and Vibration* 120 (1988) 391–406.

[8] A. Trochides, Ground-borne vibrations in buildings near subways, *Applied Acoustics* 32 (1991) 289–296.

[9] H.E.M. Hunt, Modelling of rail vehicles and track for calculation of ground-vibration transmission into buildings, *Journal of Sound and Vibration* 193 (1996) 185–194.

[10] T. Balendra, C.G. Koh, Y.C. Ho, Dynamic response of buildings due to trains in underground tunnels, *Earthquake Engineering and Structural Dynamics* 20 (1991) 275–291.

[11] S.A. Kostarev, An analysis of vibrational field, generated by an underground tunnel in soil, *Journal of Low Frequency Noise and Vibration* 15 (1996) 151–156.

[12] A.V. Metrikine, A.C.W.M. Vrouwenvelder, Surface ground vibration due to a moving train in a tunnel: two-dimensional model, *Journal of Sound and Vibration* 234 (2000) 43–66.

[13] V.V. Krylov, Low-frequency ground vibrations from underground trains, *Journal of Low Frequency Noise and Vibration* 14 (1995) 55–60.

[14] V.V. Krylov, C.C. Ferguson, Calculation of low-frequency ground vibrations from railway trains, *Applied Acoustics* 42 (1994) 199–213.

[15] D. Zhu, J. Ødegaard, On the wave propagation of ground-borne noise and vibration generated by underground trains, in: G. Guidati, H. Hunt, H. Heller, A. Heiss (Eds.), *Seventh International Congress on Sound and Vibration (ICSV7)*, Vol. V, International Institute of Acoustics and Vibration, Garmisch-Partenkirchen, Germany, 2000, pp. 2679–2686.

[16] F. Guan, I.D. Moore, Three-dimensional dynamic response of twin cavities due to travelling loads, *Journal of Engineering Mechanics, ASCE* 120 (1994) 637–651.

[17] X. Sheng, C.J.C. Jones, D.J. Thompson, Ground vibration generated by a harmonic load moving in a circular tunnel in a layered ground, *Journal of Low Frequency Noise, Vibration and Active Control* 22 (2003) 83–96.

[18] T. Balendra, K.H. Chua, K.W. Lo, S.L. Lee, Steady-state vibration of subway-soil-building system, *Journal of Engineering Mechanics, ASCE* 115 (1989) 145–162.

[19] K.H. Chua, T. Balendra, K.W. Lo, Groundborne vibrations due to trains in tunnels, *Earthquake Engineering and Structural Dynamics* 21 (1992) 445–460.

[20] W.F. Rücker, S. Said, Einwirkung von U-Bahnerschütterungen auf Gebäude; Anregung, Ausbreitung und Abschirmung [Effect of underground tunnel vibrations on buildings; propagation and screening], in: N. Chouw, G. Schmid (Eds.), *Wave Propagation and Reduction of Vibrations—Wave'94*, Berg-Verlag, Bochum, Germany, 1994, pp. 59–78.

[21] C.J.C. Jones, D.J. Thompson, M. Petyt, Studies using a combined finite element and boundary element model for vibration propagation from railway tunnels, in: G. Guidati, H. Hunt, H. Heller, A. Heiss (Eds.), *Seventh International Congress on Sound and Vibration (ICSV7)*, Vol. V, International Institute of Acoustics and Vibration, Garmisch-Partenkirchen, Germany, 2000, pp. 2703–2710.

[22] S. Wolf, Potential low frequency ground vibration (<6.3 Hz) impacts from underground LRT operations, *Journal of Sound and Vibration* 267 (2003) 651–661.

[23] R.M. Thornely-Taylor, The prediction of vibration, ground-borne and structure-radiated noise from railways using finite difference methods—Part 1—theory, *Proceedings of the Institute of Acoustics* 26 (2004) 69–79.

[24] R.M. Thornely-Taylor, The prediction of vibration, groundborne noise and structure-radiated noise using finite difference methods, in: *CD-ROM Proceedings, Eighth International Workshop on Railway Noise (IWRN8)*, Buxton, Derbyshire, UK, 2004.

[25] W. Gardien, H.G. Stuit, Modelling of soil vibrations from railway tunnels, *Journal of Sound and Vibration* 267 (2003) 605–619.

[26] L. Andersen, C.J.C. Jones, Coupled boundary and finite element analysis of vibration from railway tunnels—a comparison of two- and three-dimensional models, in: *CD-ROM Proceedings, Eighth International Workshop on Railway Noise (IWRN8)*, Buxton, Derbyshire, UK, 2004.

[27] X. Sheng, C.J.C. Jones, D.J. Thompson, Prediction of ground vibration from trains using the discrete wavenumber finite and boundary element methods, in: *CD-ROM Proceedings, Eighth International Workshop on Railway Noise (IWRN8)*, Buxton, Derbyshire, UK, 2004.

[28] G. Degrande, P. Chatterjee, D. Clouteau, T. Al-Hussaini, M. Arnst, R. Othman, A numerical prediction model for ground-borne vibrations from underground railway traffic using a coupled periodic FEM-BEM approach, in: A.C. Nilsson, H. Boden (Eds.), *Tenth International Congress on Sound and Vibration (ICSV10)*, Vol. 1, International Institute of Acoustics and Vibration, Stockholm, Sweden, 2003, pp. 395–402.

[29] D. Clouteau, R. Othman, M. Arnst, H. Chebli, G. Degrande, R. Klein, P. Chatterjee, B. Janssens, A numerical model for ground-borne vibrations from underground railway traffic based on a periodic FE-BE formulation, in: *CD-ROM Proceedings, Eighth International Workshop on Railway Noise (IWRN8)*, Buxton, Derbyshire, UK, 2004.
[30] D. Clouteau, M. Arnst, T.M. Al-Hussaini, G. Degrande, Freefield vibrations due to dynamic loading on a tunnel embedded in a stratified medium, *Journal of Sound and Vibration* 283 (2005) 173–199.
[31] D. Clouteau, M.L. Elhabre, D. Aubry, Periodic BEM and FEM-BEM coupling: application to seismic behaviour of very long structures, *Computational Mechanics* 25 (2000) 567–577.
[32] P. Chatterjee, G. Degrande, S. Jacobs, J. Charlier, P. Bruvet, D. Brassenx, Experimental results of free field and structural vibrations due to underground railway traffic, in: A.C. Nilsson, H. Boden (Eds.), *Tenth International Congress on Sound and Vibration (ICSV10)*, Vol. 1, International Institute of Acoustics and Vibration, Stockholm, Sweden, 2003, pp. 387–394.
[33] G. Degrande, P. Chatterjee, R. Klein, W. Van de Velde, P. Hölscher, V. Hopman, A. Wang, N. Dadkah, Vibrations due to a test train at variable speeds in a deep bored tunnel embedded in London clay, in: *CD-ROM Proceedings, Eighth International Workshop on Railway Noise (IWRN8)*, Buxton, Derbyshire, UK, 2004.
[34] W. Flügge, *Stresses in Shells*, second ed., Springer, Berlin, 1973.
[35] A. Leissa, *Vibration of Shells*, Acoustical Society of America, New York, 1973 (reissued 1993).
[36] D.C. Gazis, Three-dimensional investigation of the propagation of waves in hollow circular cylinders. I. Analytical foundation, *Journal of the Acoustical Society of America* 31 (1959) 568–573.
[37] U.G. Köpke, Transverse vibration of buried pipelines due to internal excitation at a point, *Proceedings of the IMechE, Part E: Journal of Process Mechanical Engineering* 207 (1993) 41–58.
[38] K.F. Graff, *Wave Motion in Elastic Solids*, Oxford University Press, London, 1975.
[39] S. Timoshenko, J.N. Goodier, *Theory of Elasticity*, third ed., McGraw-Hill, New York, 1970.
[40] G.N. Watson, *A Treatise on the Theory of Bessel Functions*, second ed., Cambridge University Press, London, 1966.
[41] E. Kreyszig, *Advanced Engineering Mathematics*, sixth ed., Wiley, New York, 1988.
[42] A. Tuchinda, Underground Vibration, Fourth-year project report, Department of Engineering, University of Cambridge, 1998.
[43] R.D. Blevins, *Formulas for Natural Frequency and Mode Shape*, Krieger Publishing Company, Malabar, Florida, USA, 1979 (reissued 1993).
[44] L. Meirovitch, *Elements of Vibration Analysis*, second ed., McGraw-Hill, New York, 1986.
[45] F.W.J. Olver, Bessel functions of integer order, in: M. Abramowitz, I.A. Stegun (Eds.), *Handbook of Mathematical Functions*, Dover Publications, New York, 1972, pp. 355–433.
[46] H.E.M. Hunt, Measurement and Modelling of Traffic-induced Ground Vibration, PhD Thesis, University of Cambridge, 1988.
[47] K.-H. Xie, G.-B. Liu, Z.-Y. Shi, Dynamic response of partially sealed circular tunnel in viscoelastic saturated soil, *Soil Dynamics and Earthquake Engineering* 24 (2004) 1003–1011.